Large-scale bipolar outflow from the galactic nucleus of M106.

Yuxuan Zeng

University of Groningen

Large-scale bipolar outflow from the galactic nucleus of M106

Master's Thesis

To fulfill the requirements for the degree of
Master of Science in Astronomy
at University of Groningen under the supervision of
Prof. dr. F. Fraternali (Astronomy, University of Groningen)
and
Prof. Q, Daniel Wang (Astronomy, University of Massachusetts Amherst)

Yuxuan Zeng (s4625684)

July 4, 2023

Contents

Acknowledgments

Abstract

In this study, I investigate the role of energetic outflows from galactic nuclei in shaping galaxy formation and evolution, a topic that is still surrounded by uncertainty. My focus is on the nearby disk galaxy M106 (NGC4258), where I present compelling evidence for a large-scale bipolar structure emitting radio and X-ray radiation. By analyzing recently released Low-Frequency Array (LoFAR) survey data and archival observations from the Chandra X-ray Observatory, I aim to gain insights into the underlying physical mechanisms driving this enigmatic structure.

Similar to the well-known the eROSITA/Fermi bubbles in our own Galaxy, the M106 bubbles enclose diffuse hot plasma and exhibit prominent radio and X-ray emitting edges. Through mapping the distribution of radio spectral indices and constraining the magnetic field strength, I unveil intriguing details about the inner workings of the structure. My analysis reveals a magnetic field strength varying from approximately $4\mu G$ to $13\mu G$, transitioning from the centers to the edges of the M106 bubbles, assuming energy equipartition between cosmic rays and the magnetic field.

Furthermore, the diffuse X-ray emission from the bubbles' spectrum offers additional insights, indicating the presence of Ne, Mg, and Si He-α lines. I estimate the thermal energy associated with the entire structure to be approximately 3×10^{56} erg, likely originating from the low-luminosity active galactic nucleus (AGN) of the galaxy in the recent past. However, my analysis indicates that the current energy input from the AGN's jets is insufficient, and their orientation is not aligned with the bipolar structure.

Additionally, I present evidence for diffuse X-ray emission on larger scales, suggesting the existence of a hot galactic corona. These findings collectively demonstrate the significant role of energetic galactic nuclear feedback in regulating the properties of circumgalactic medium of disk galaxies, including those akin to our own.

Overall, this study provides a comprehensive examination of the M106 bipolar structure, shedding light on the complex processes associated with energetic outflows from galactic nuclei. The results contribute to our understanding of galaxy formation and evolution, emphasizing the influence of galactic nuclear feedback on the circumgalactic environment.

1   Introduction

1.1   Galactic feedback

Galactic feedback is a fundamental process in astrophysics that involves the intricate interplay between matter and energy flows within and out of galaxies (Fig. 1). It refers to the various mechanisms through which galaxies regulate their star formation and gas content by expelling matter and energy into their surroundings. Galactic feedback can take different forms, such as supernova explosions, stellar winds, and radiation from active galactic nuclei (AGN), and can inject considerable amounts of energy into the interstellar medium (ISM) and the circum-galactic medium (CGM). This energy injection drives shocks and turbulence that influence the dynamics and thermal properties of the gas, newly formed metals in stellar interiors and supernova explosions are also spread around with key consequences for the chemistry of both ISM and CGM. The combination of these phenomena shape the properties of galaxies such as their stellar populations, morphology, and gas content over cosmic time. As such, understanding the mechanisms and effects of galactic feedback is crucial for comprehending the formation and evolution of galaxies in the universe (e.g., McKee & Ostriker, 1977; Heckman & Best, 2014; Hopkins et al., 2014; Tumlinson et al., 2017).

AGN feedback, can have a significant impact on the evolution of galaxies and the quenching of their star formation. Stars form from gas and dust that cools and condenses, leading to nuclear fusion and the production of heavier elements. However, when AGN feedback occurs, the central AGN heats up the gas in the surrounding medium, preventing it from cooling and condensing, and thus inhibiting star formation. AGN-driven outflows can also contribute to the removal of significant amount of gas from the ISM (Ishibashi & Fabian, 2016; Zubovas & Bourne, 2017). All this can result in a scenario of quenching, where star formation is greatly reduced or completely halted (Schawinski et al., 2014). Understanding how AGN feedback affects star formation is essential for understanding the evolution of galaxies over cosmic time (Martig et al., 2009; Fabian, 2012a).

AGN feedback also plays a crucial role in regulating the growth of supermassive black holes (SMBH) itself, located in the nucleus of the host galaxy. These black holes expand through a process known as accretion, where matter is drawn into the black hole by gravity. As gas accumulates, it forms an optically thick disk called an accretion disk (Shakura & Sunyaev, 1973; Hickox & Alexander, 2018). The commonly used spherically symmetric model for accretion leads to a limit in the accretion rate that is called Eddington limit (Rybicki & Lightman, 1986; Woo & Urry, 2002).

In many cases, the accretion luminosity of an AGN remains below the Eddington limit. However, it is also possible for super-Eddington luminosity and mass accretion rates to occur, particularly when the accretion process is not spherically symmetric (Bondi, 1952; Cimatti et al., 2019). Accretion in AGNs can occur in two distinct modes: the quasar mode and the radio mode. In the quasar mode, accretion takes place at a high rate, approaching the Eddington limit. In contrast, the radio mode involves low accretion rates, significantly below the Eddington limit, due to the presence of hot gas at the virial temperature within the host system. AGN feedback, encompassing both radiative and mechanical forms, acts as a regulatory mechanism on the accretion process. As the AGN heats up the surrounding gas via radiation and shocks, it then exerts additional pressure that drives the gas away, thereby reducing the inflow of material and restricting the black hole's accretion rate (e.g. Fabian, 2012b).
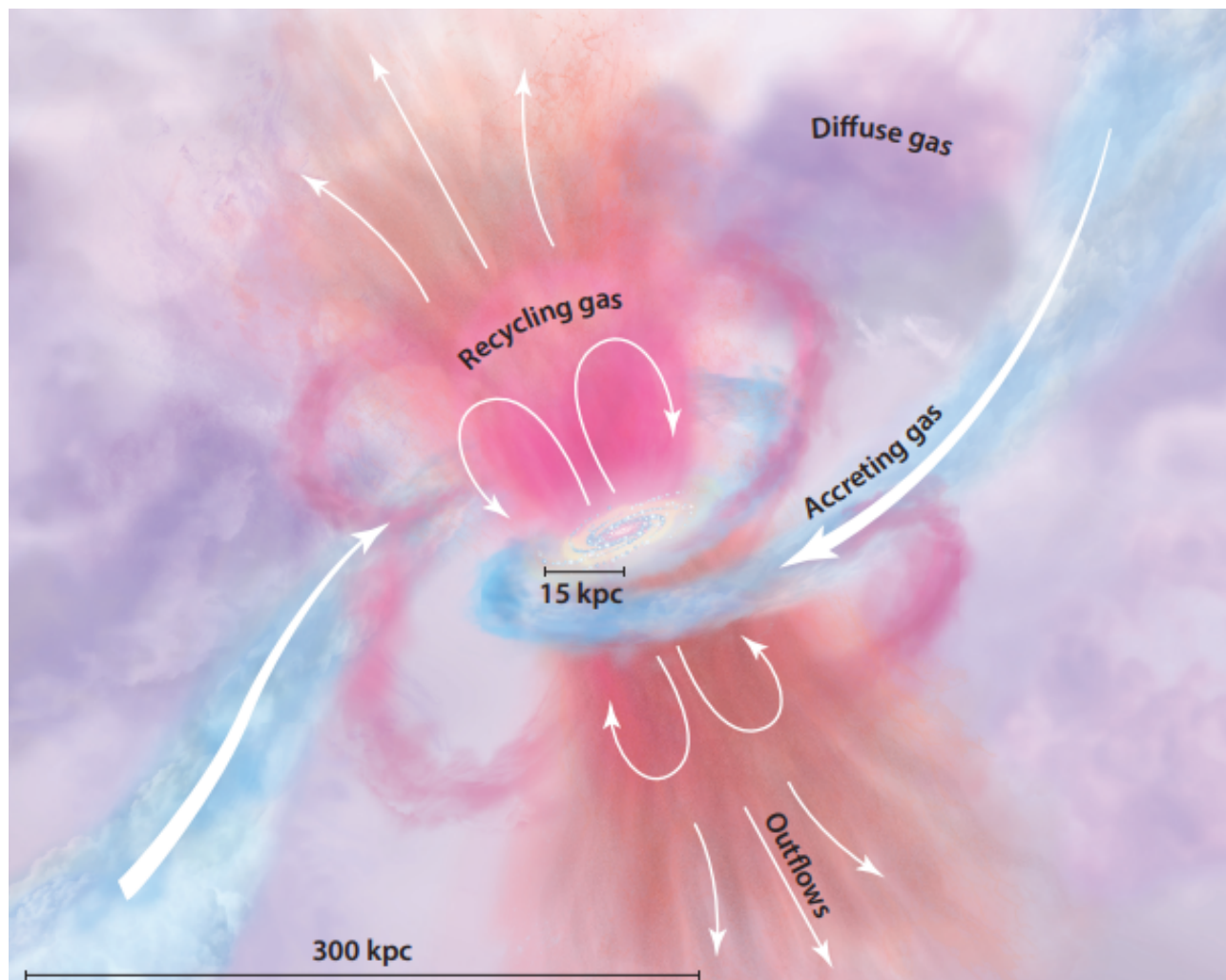
Figure 1: This is a visual representation from the Tumlinson et al. (2017) showcasing the matter and energy flows within the circum-galactic medium (CGM). The inflow is depicted as accreting gas, displayed in blue, while the outflow and recycling gas are represented in red.

1.2 Fermi/eROSITA bubbles

In 2010, the Fermi Gamma-ray Space Telescope detected an unexpected and striking feature in the gamma-ray emission from the Milky Way (Fig. 2): two large, bipolar bubbles extending from the Galactic Center above and below the Galactic plane. The discovery was made using the Large Area Telescope (Fermi-LAT), which revealed the structure in high-energy gamma rays. The Fermi bubbles are among the largest structures in our Galaxy, with a size of approximately 10 kiloparsecs (Su et al., 2010). Decades later the eROSITA (Extended Roentgen Survey with an Imaging Telescope Array) X-ray telescope detected a similar structure to the Fermi bubbles in the X-ray emission from the Milky Way (Fig. 3). The eROSITA telescope is a German-led project that is designed to conduct an all-sky survey in the X-ray regime. The newly discovered X-ray bubbles in addition to the previous known ROSAT North Polar Spur (Large et al., 1962; Snowden et al., 1995) have a similar bipolar morphology to the Fermi bubbles and extend to a greater distance from the Galactic plane, about 14 kiloparsecs (Predehl et al., 2020). Part of the X-ray/Gamma-ray bubbles also shown prominent radio

counterparts recognised as Radio Loop I (Berkhuijsen, 1971; Carretti et al., 2013).

The origin of the Fermi/eROSITA bubbles continues to be an active area of research, with multiple hypotheses proposed to explain their formation. A compelling hypothesis is the supernova feedback scenario, which suggests that they are the results of shock-heated gas resulting from supernova explosions in the central Galactic regions. This process potentially creates cavities that give rise to the observed bubbles. The Central Molecular Zone (CMZ) stands out as a distinct region containing a large amount of gas and hosting massive young star clusters and a significant number of supernovae. High star formation activities in the CMZ and Galactic nucleus are likely driven by the non-axisymmetric gravitational field of the Galactic bar (Carretti et al., 2013; Crocker et al., 2015; Henshaw et al., 2022).
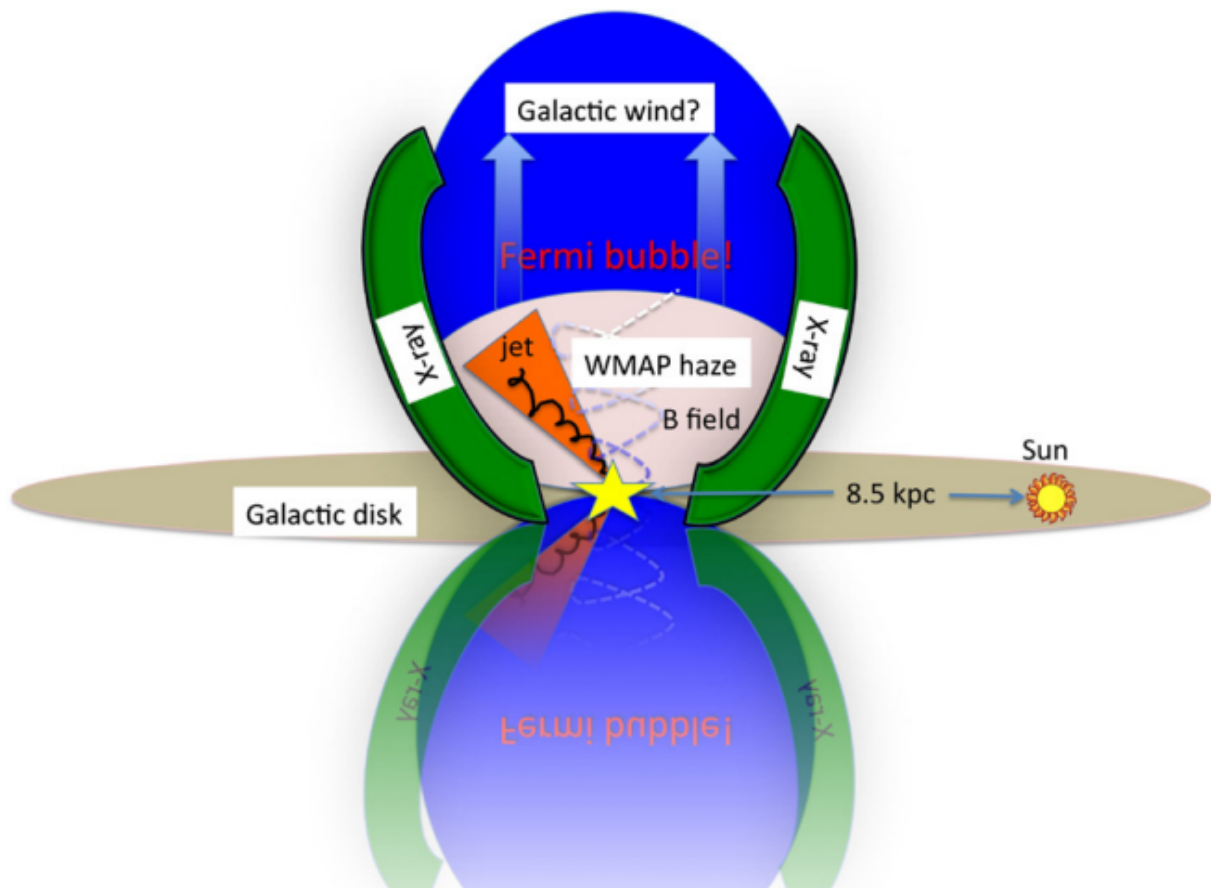

Figure 2: This is an illustration from Su et al. (2010), displaying the Fermi bubbles - two large bubbles detected in Fermi-LAT above and below the galactic plane. The green arcs depict the ROSAT X-ray emissions surrounding the Fermi bubbles, while the Sgr A* is indicated as stars at the center of the image.
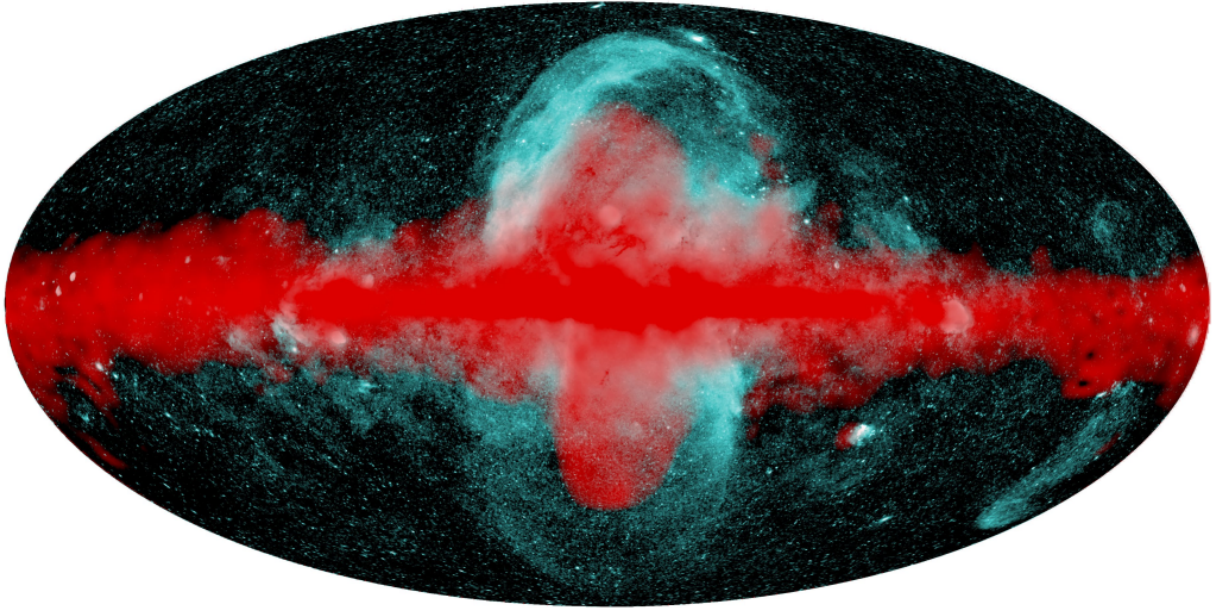
Figure 3: This is Fig. 3 from the Predehl et al. (2020), depicting a composite image of the Fermi and eROSITA bubbles. The soft X-ray emissions in the energy band of 0.6-1 keV are shown for the eROSITA bubbles. The Fermi observation is represented in red, while the eROSITA observation is displayed in cyan.

The other hypotheses regarding the origin of the Fermi/eROSITA bubbles is AGN feedback, which involves jets or other forms of energetic outflows emanating from the central AGN (Sgr A*) of our Milky Way. Located approximately 8 kpc away from us, the supermassive black hole at the center of the Milky Way has a mass of $4 \times 10^6 M_\odot$ (Gillessen et al., 2009). Feedback from Sgr A* could have generated powerful streams of gas and radiation, potentially leading to the shock heated gas envelop and the formation of the observed bubbles. Independently of their origin, it is clear that the tremendous energy of the bubbles, estimated to be around 10^{56} erg, has significantly impacted the structure, energy content, and chemical enrichment of the circumgalactic medium in our Milky Way (Guo & Mathews, 2012; Yang et al., 2012; Zubovas & Nayakshin, 2012; Yang et al., 2022).

1.3   LoFAR Observations

The Low-Frequency Array (LOFAR) is a remarkable instrument that can detect radio signals from a vast portion of the visible sky. The dipole arrays utilized by LOFAR have an extensive field of view, capable of covering hundreds of square degrees at the lowest frequencies detectable by the instrument. ASTRON operates this international telescope across various locations in Europe, as illustrated in Fig. 4. LOFAR comprises two different antennas: the High Band Antennas (HBA, 110-240 MHz) and Low Band Antennas (LBA, 10-90 MHz). To exploit the potential of these antennas, several surveys have been conducted, including the Multifrequency Snapshot Sky Survey (MSSS), which surveyed the entire northern sky to a depth of 10 Jy/beam with a resolution of 2 arcminutes (Heald et al., 2015); the LOFAR Two-metre Sky Survey (LoTSS), currently conducting a survey of the entire northern sky at a wavelength of 120-168 MHz with a sensitivity of 100 μJy/beam and a resolution of 6 arcseconds (Shimwell et al., 2017, 2022). The LoTSS deep field, which covers the same area as the LoTSS wide area, has a sensitivity of 10 μJy/beam. Additionally, the LOFAR LBA

Sky Survey (LoLSS) covers the entire northern sky in the range of 42-66 MHz, with a resolution of 15 arcseconds and a noise level of 1 mJy/beam (Shimwell et al., 2019).
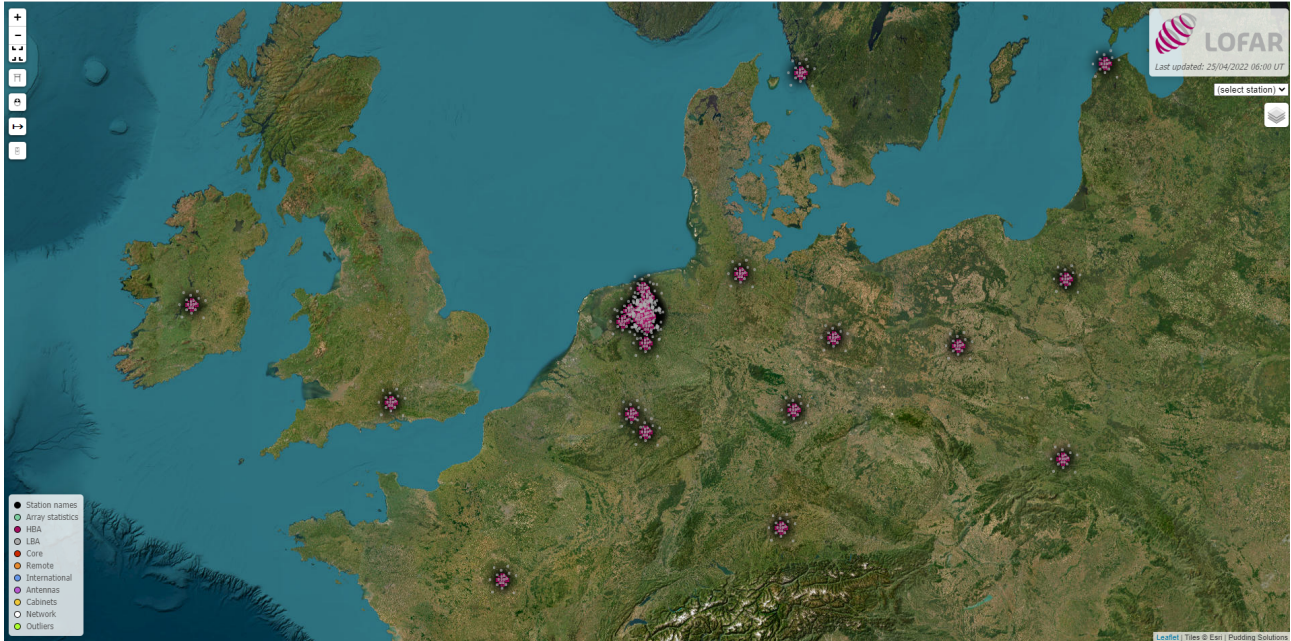
Figure 4: This map https://www.astron.nl/lofartools/lofarmap.html displays the locations of antennas used in the Low-Frequency Array (LOFAR) across Europe. The HBA antennas are marked in magenta, while the LBA antennas are marked in grey.

1.4   Chandra Observations

The Chandra X-ray observatory (Fig. 5), launched on July 23, 1999, is NASA's flagship mission for X-ray astronomy. X-rays are absorbed by the Earth's atmosphere (as shown in Fig. 6), so Chandra orbits at an altitude of 139,000 km in space. The Chandra X-ray Center is hosted by the Smithsonian's Astrophysical Observatory in Cambridge, MA.

There are two distinct instruments on the Chandra telescope, namely the Advanced CCD Imaging Spectrometer (ACIS) and the High Resolution Camera (HRC). In our study, we specifically utilize the ACIS instruments, focusing on the ACIS-S S3 chips (referred to as CCD 7 in Figure 7). These chips are of the back-illuminated (BI) CCD type, while there are also front-illuminated (FI) CCDs available. The main differences between the two can be characterized as follows: the response of the BI devices extends to energies below what the FI chips can detect, and the chip-average energy resolution of the BI devices is superior to that of the FI devices.
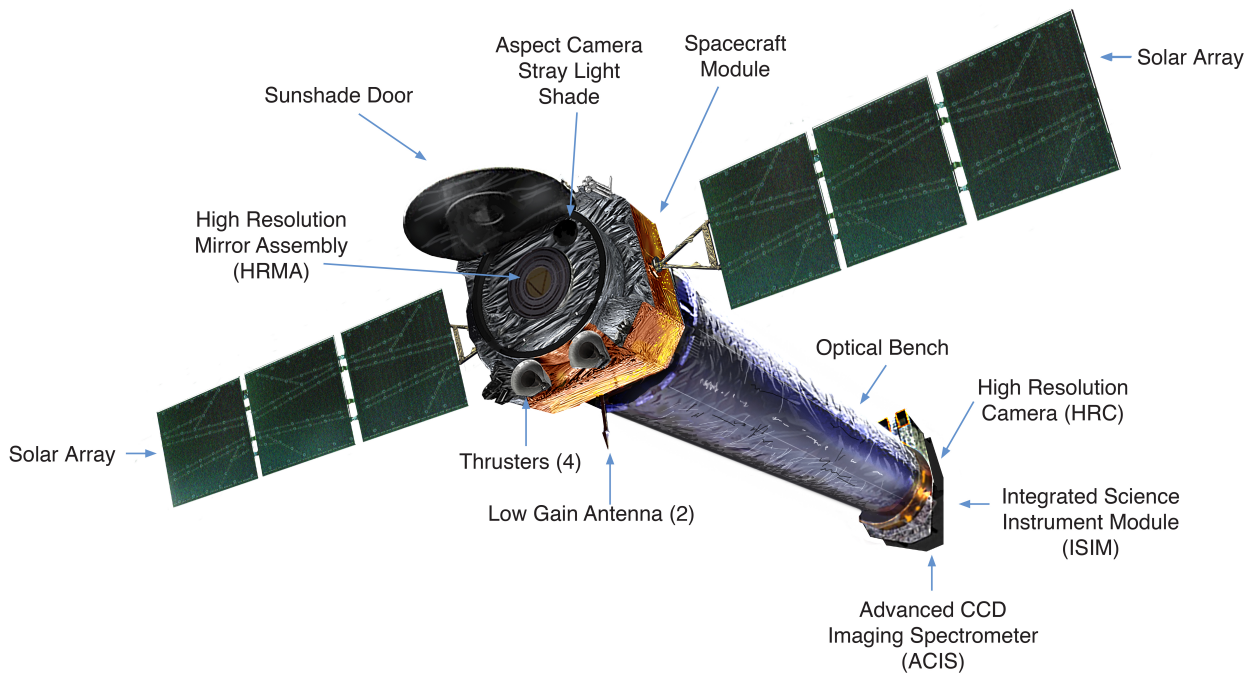
Figure 5: This image shows the components of the Chandra space telescope, including various instruments used in different areas of high energy astrophysics. The Chandra X-ray Observatory utilizes two main instruments: the Advanced CCD Imaging Spectrometer (ACIS) and the High Resolution Camera (HRC).
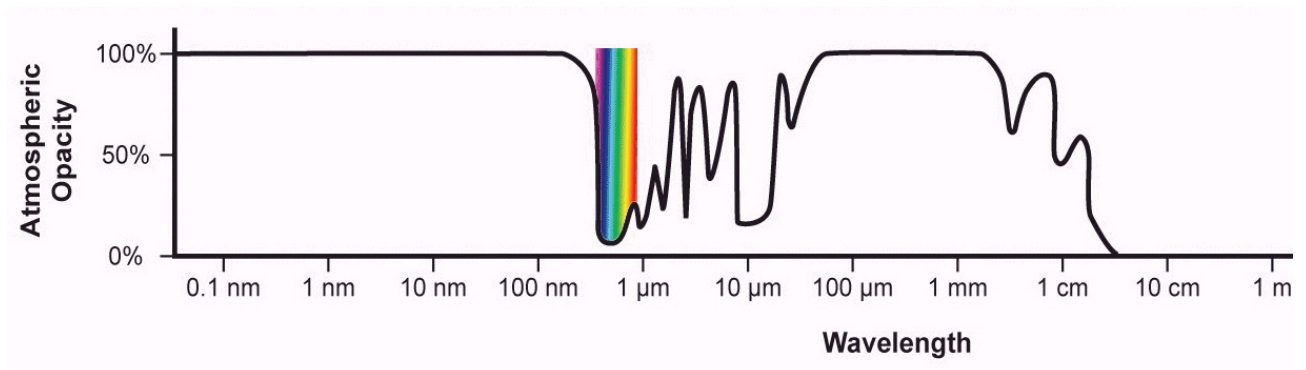
Figure 6: This image, credited to https://cimss.ssec.wisc.edu/sage/remote_sensing/lesson2/atm_op.htm, illustrates how the Earth's atmosphere absorbs different forms of light. As radio and visible light are not absorbed, they can be observed from ground-based observatories. In contrast, other forms of light require space-based observatories, in particular X-ray and gamma rays.

ACIS FLIGHT FOCAL PLANE
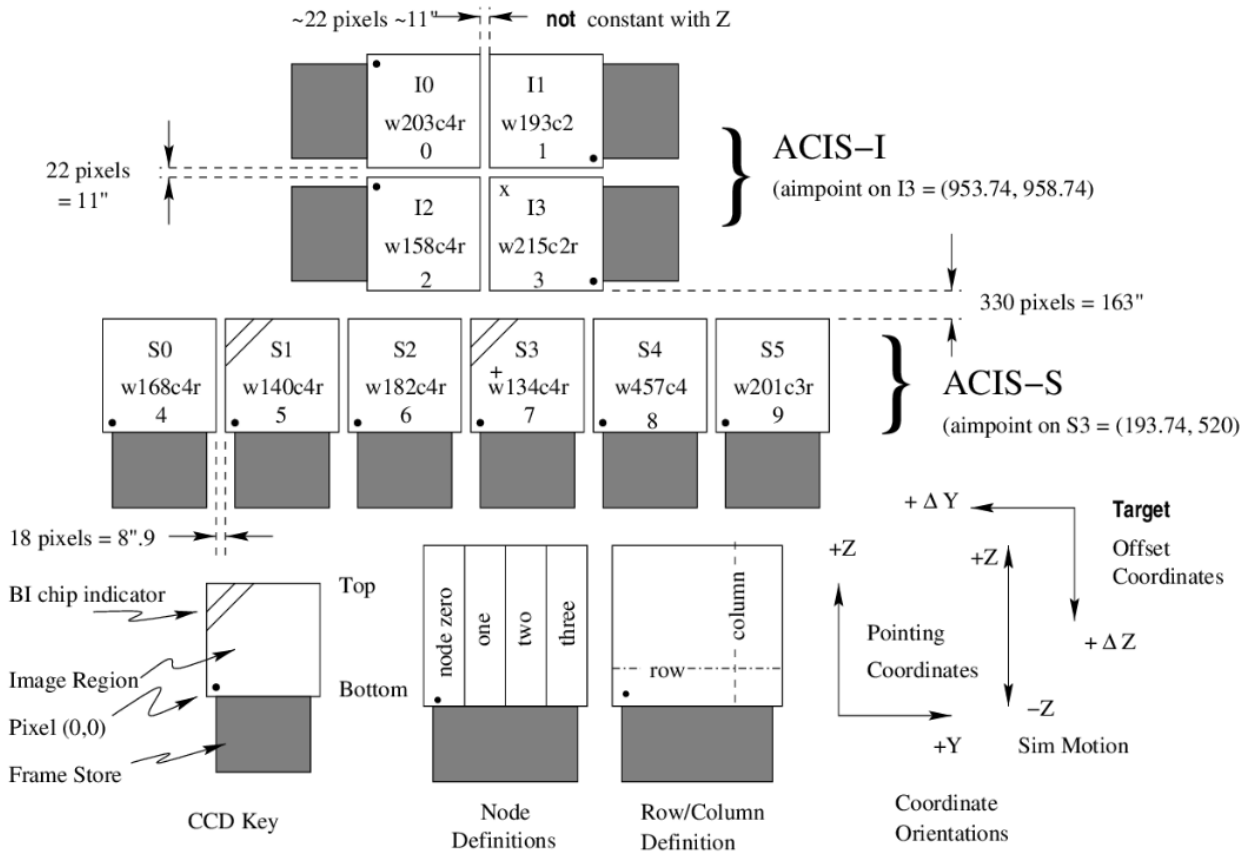
Figure 7: The ACIS instrument on the Chandra X-ray Observatory is composed of two types of CCD chips. The top four CCDs are labeled I0-I3 and are known as the ACIS-I chips, while the bottom six CCDs are labeled S0-S5 and are referred to as the ACIS-S chips.

1.5   The nearby disk galaxy M106

In this thesis, I have studied the LOFAR and X-ray emissions of M106, which is a neaby disk galaxy, classified as SABc and seen at a high inclination angle with respect to our line of sight. M106 has undergone comprehensive studies across various wavelengths, revealing the presence of a "low-luminosity" AGN that shares similarities with typical Seyfert galaxies (Makishima et al., 1994). Furthermore, the central AGN in M106 is surrounded by highly luminous water masers, making it one of the most luminous targets of its kind. These bright water masers orbiting the AGN provide valuable insights into the energetic processes occurring within M106 and excellent estimate of black hole mass of $3.6 \times 10^7 M_\odot$ (Claussen et al., 1984; Miyoshi et al., 1995; Bragg et al., 2000). M106 exhibits properties similar to our own Milky Way. Both have well-defined spiral arms extending from their bulges. They are comparable in size and luminosity. Additionally, both galaxies harbor a stellar bar in their central region although the Milky Way's bar is more extended. The salient parameters of this neighboring disk galaxy are presented in Table 1. To provide a sense of scale, at a distance of M106, $1'$ corresponds to approximately 2.22 kpc.
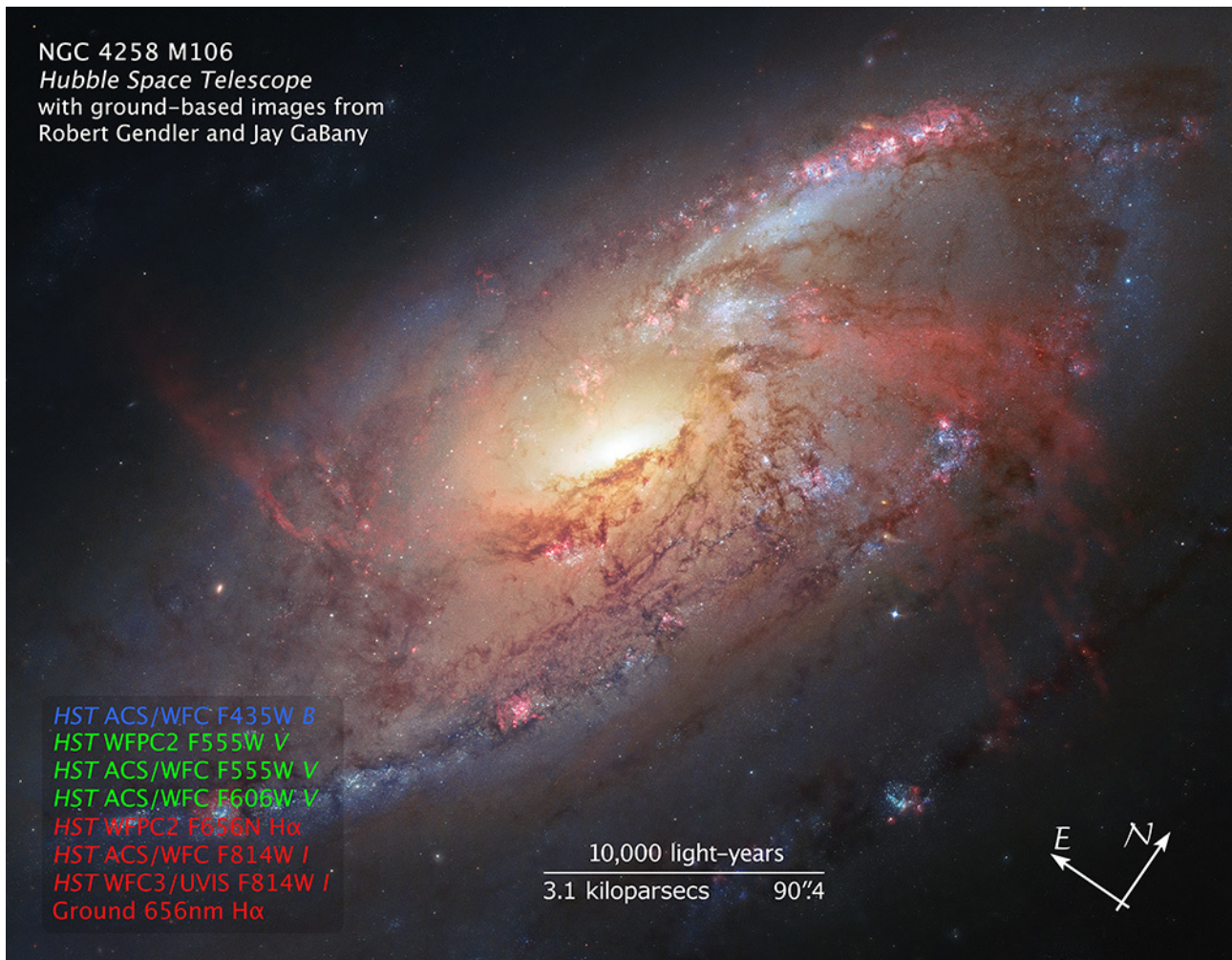
Figure 8: Composite image of M106 combining multi-color observations from the Hubble Space Telescope (HST) and ground-based H α observations https://hubblesite.org/contents/media/images/2013/06/3143-Image.html reveals a normal galaxy disk with spiral arms spanning north to south, while a striking red (H-alpha) "anomalous" arm deviates significantly from the expected spiral pattern.

One distinguishing feature of M106 is the presence of bright "anomalous" arms (see Fig. 8), which deviate significantly from the normal spiral arms (van der Kruit et al., 1972). These anomalous arms have been observed in multiple wavelengths, including radio, H_α, and X-ray, suggesting that they are formed by gas shock heated by the powerful jets (e.g., Yang et al., 2007). Extensive research has focused on studying these anomalous arms, as well as investigating the low luminosity obscured AGN, which emits approximately 10^{40} ergs s^{-1} in the 2-10 keV energy range, along with its associated jets (e.g., Makishima et al., 1994; Lasota et al., 1996; Véron-Cetty & Véron, 2006; Masini et al., 2022). Additionally, investigations have explored the normal spiral arm and the Galactic disk. Notably, studies have revealed that the cold molecular gas estimated from the CO emission is ten times larger than that estimated from dust emission. This would mean that either the gas/dust ratio is estimated to be 10 times smaller compared to the Milky Way, or the estimated X_{CO} factor is 10 times lower. The conclusive result indicates that X_{CO} is significantly reduced by a factor of 10, primarily due to the high temperature and turbulence inside the jet-shocked anomalous arms. The jet's high-energy deposition leads to the inflation of a cocoon comprised of hot gas. This cocoon has the capability to envelop

and shock the entirety of the host galaxy's interstellar medium (ISM). As a consequence, disk gas is ejected into the halo through X-ray overflow (Laine et al., 2010; Ogle et al., 2014).

1.6   Research Motivation and Candidate

The discovery of Fermi/eROSITA bubbles in the Milky Way has gained significant attention; however, the origin, formation, and evolution of these large-scale bipolar superbubble structures remain unclear. In order to better understand galactic nuclear outflows and their interactions with the circumgalactic medium, we have identified M106 as a promising candidate for further investigation.

We present the detection of a bipolar superbubble structure, apparently driven by AGN, in M106, using both Chandra X-ray and LoFAR radio data. For ease of reference, Fig. 9 illustrates the main components of the galaxy that are of interest in this thesis. The anomalous arms are thought to be produced by the jets, although they are currently pointing in directions quite different from the orientation of the superbubble structure and terminate at much smaller scales, as represented by the radio hot spots (Cecil et al., 2000; Yang et al., 2007) in Fig. 9. We find that the anomalous arms represent only the southern and northern parts of the outer boundaries of the radio/X-ray east (E) and west (W) bubbles (Figs. 9-11). These edge-brightened parts of the two bubbles are hereafter referred to as the E and W edges. Below the W edge there is also inner radio arm presented and it is connecting to the N hot spot which can also be seen in high resolution Radio observations (e.g. Cecil et al., 1995). Such unilaterally enhanced radio/X-ray edges are also present in or around the eROSITA/Fermi bubbles, although line-of-sight confusion with other features in the Galactic disk has prevented a firm physical association (e.g., Das et al., 2020; Panopoulou et al., 2021). With the moderate inclination angle of the M106 disk (Table 1) such confusion is small. So the physical association of the anormalous arms with the bubbles is quite clear. In short, M106 now provides us with a new perspective to study the formation and evolution of the large-scale bipolar superbubble structure, which is probably the best known case for studying the interplay of galactic nuclear outflows with the CGM in a nearby disk galaxy.

1.7   Thesis Outline

The thesis is organized as follows: Chapter 2 focuses on the description of the data reduction process for both the radio and X-ray data, starting from the LoFAR data release and Chandra Events files. We delve into the details of the imaging and spectral analysis specifically for the X-ray data. In Chapter 3, we present our findings, encompassing the results obtained from both the imaging and spectral analyses.

Chapter 4 revolves around a comprehensive discussion of the implications of our results. We compare our findings with similar features observed in other galaxies, with a particular emphasis on the eROSITA/Fermi bubbles. Additionally, we examine the relevance of our results in light of cosmological simulations, as they provide a significant basis for comparison.

Finally, in Chapter 5, we provide a concise summary of the main discoveries and contributions of this work. This includes an overview of the bubble's size, emission properties, magnetic field strength, age, energy, and other relevant aspects.

Table 1: Parameters of M106

Parameter	Values
Galaxy Name	M106, NGC4258
Type	SABc
Distance (Mpc)	7.6
M_B (mag)	5-20.59
$M_*(10^{10}\ M_\odot)$	8.2
SFR ($M_\odot\ yr^{-1}$)	1.4
Disk incl. (deg)	71°
Disk rotation (km s^{-1})	208
$N_{H,G}(10^{20}\ cm^{-2})$	4.21

Note: Parameters are obtained from NED/SIMBAD, except for the Type and magnitude from Heald et al. (2011), stellar mass (M_*) from (Burbidge et al., 1963), foreground Galactic HI column density ($N_{H,G}$) from (HI4PI Collaboration et al., 2016), and star formation rate (SFR) from (Ogle et al., 2014).
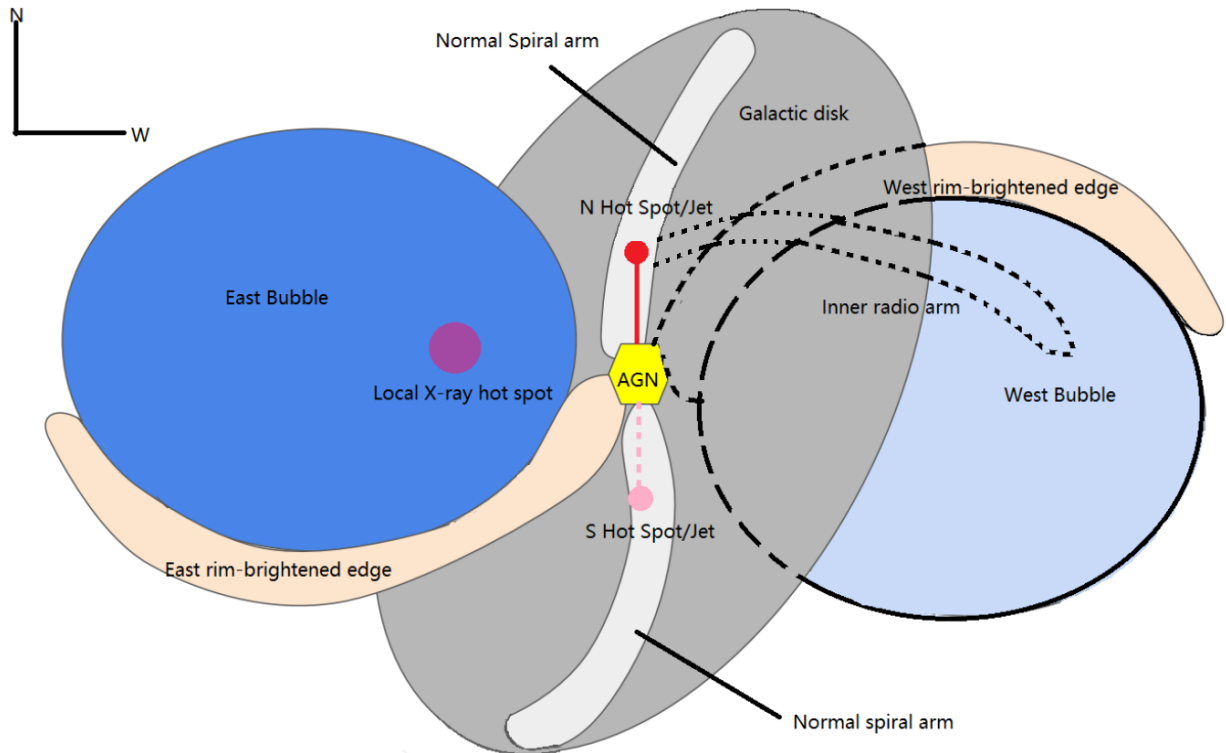
Figure 9: Illustration of the main components of the M106 concerned in the present work: the galactic disk as seen optically; the east and west radio/X-ray emitting bubbles reported here, consisting of both their interiors (represented by the two ellipses) and their rim-brightened outer edges, previously known as the two major anomalous arms. In addition, the inner arm is marked and connected to the N hot spot which could be seen in high resolution radio image (e.g. Cecil et al., 1995) The inclined disk has its near side in front of the western part of this bipolar superbubble structure, apparently originating from the AGN, which is also marked together with two radio-observed jets.

2   Data reduction and analysis

The later chapters of this thesis are based on the submitted paper "Tracing the Energetic Outflows from Galactic Nuclei: Observational Evidence for a Large-Scale Bipolar Radio and X-ray-emitting Bubble-like Structure in M106", Zeng et al., MNRAS, 2023, submitted

2.1   LoFAR data

The present work began with an examination of the recently released LoFAR data. The data cover M106 in both the 41-66 MHz band (with an effective center frequency of $\nu_1 = 54$ MHz and a resolution of $15''$ FWHM) and the 120-168 MHz band ($\nu_2 = 144$ MHz and $6''$) from the LoFAR LoLSS DR1 (de Gasperin et al., 2023) and the LoFAR LoTSS DR2 (Shimwell et al., 2022), respectively. The released survey data (Fig. 10) are of sufficiently high quality to study both the overall morphology and the intensity distributions of the substructures.

We further reduce the data to map the spectral index of the radio emission. First, we convolve the 144 MHz image to the resolution of the 54 MHz image. Second, we remove from each image a local background – the median intensity in a "clean" neighborhood of M106 (Fig 10): $80\,\mu\mathrm{Jy\,arcsec^{-2}}$ at 54 MHz or $15\,\mu\mathrm{Jy\,arcsec^{-2}}$ at 144 MHz. Third, the root mean square (RMS) of the intensity in the region, 10 and 12 $\mu\mathrm{Jy\,arcsec^{-2}}$, is used as the noise estimate for the background subtracted 54 and 144 MHz images. Fourth, only the field with a signal-to-noise ratio (S/N) greater than 3 in both images, further excluding regions contaminated by discrete compact radio sources, is retained for the calculation of the spectral index, which is defined as

$$\alpha = -\frac{\ln(S_2/S_1)}{\ln(\nu_2/\nu_1)}, \tag{1}$$

where S_1 and S_2 are the intensities at the two frequencies. When calculating the average spectral index of a region, we estimate its error as the RMS divided by the square root of the number of covered beams (FWHM$= 15''$).

We also try to isolate the radio emission of the galactic disk from that of the bipolar structure. This is especially useful for a more accurate calculation of the spectral index of the radio emission from the M106 structure. To do this we use a WISE $22\mu m$ intensity image of the galaxy to trace the radio contribution from the galactic disk. (The ability to calibrate radio emission as an indicator of star formation rate (SFR) is attributed to the extensively researched infrared-radio correlation (IRRC).(Delvecchio et al., 2021)) The image, downloaded from the InfraRed Science Archive (IRSA) [1], contains a strong background. We estimate it in the same off-galaxy field as marked in Fig. 10 and subtract it from the whole image. The resulting net $22\mu m$ emission from the galaxy should be mostly due to dust-reprocessed UV radiation from massive stars. Their feedback is also expected to be responsible for the acceleration of the cosmic ray particles producing much of the radio emission from the disk. The WISE $22\mu m$ intensity may not exactly follow the synchrotron radiation, because the underlying diffusion or transfer processes of cosmic ray particles and UV radiation may be quite different. However, we find that an approximate subtraction of the disk contribution is sufficient to test its effect on the radio index calculation. In each of the two LoFAR bands, we adjust the ratio of radio

---

[1]https://irsa.ipac.caltech.edu/Missions/wise.html
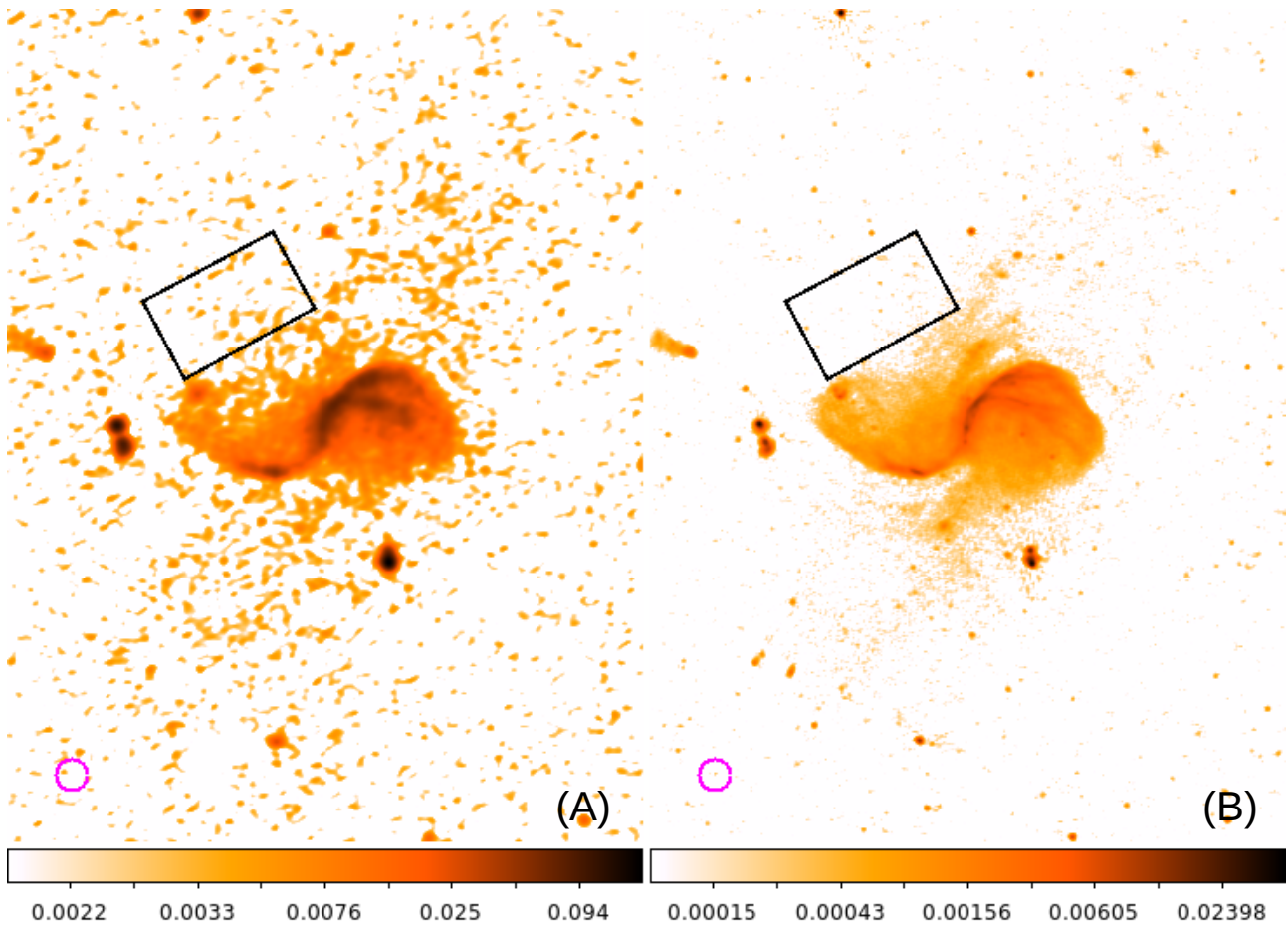
Figure 10: LoFAR intensity images of M106 in units of Jy beam^{-1} at the 54 MHz (left) and 144 MHz (right). The magenta circle in the lower left corner illustrates the 1 kpc radius at the distance of the galaxy, while the outlined rectangular region is used to estimate the background and its RMS. The scale contrast in panel B is lower than panel A to better show the bubble.

to $22\,\mu m$ intensity so that the radio image looks uniform over the disk regions after subtracting the disk contribution (Fig 12). The ratios of the two LoFAR bands are then used to estimate the mean spectral index (0.84 ± 0.07) of the disk. With the resulting disk-subtracted images, we rebuild the radio spectral index map. We find that the effect on the radio index calculation is quite small.

2.2   Chandra data

2.2.1   Data selection and calibration

Our X-ray study of M106 uses the same two Chandra observations described in Yang et al. (2007) (see also Table 2). These observations were made with the Advanced CCD Imaging Spectrometer-Spectroscopy (ACIS-S). We use only the data collected by the S3 CCD chip, which covers M106. Fig. 13A shows the effective exposure map of the combined data. We use the Chandra Interactive Analysis of Observations (CIAO) software (version 4.14 with CALDB 4.9.7) to process the data, following the standard procedure which includes the cleaning of time intervals with strong background flares using the DEFLARE tool, and the merging of the count and exposure images to produce the mosaic maps in the 0.45-1, 1-2, and 2-7 keV bands, as well as the broad (0.45-7 keV) bands.
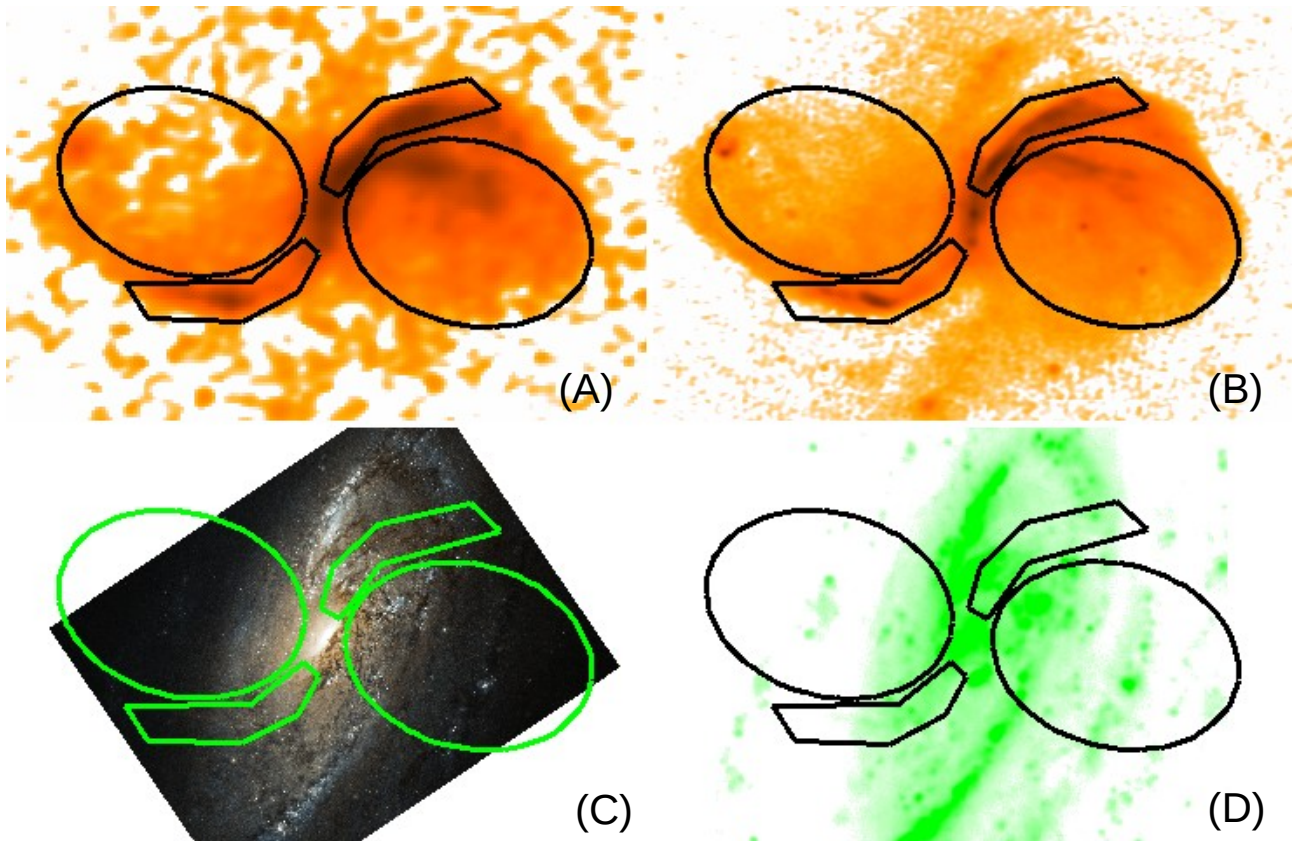
Figure 11: Radio detection of the bipolar superbubble structure in M106: (A) LoLSS DR1 54 MHz and (B) LoTSS DR2 144 MHz images of the galaxy. The interiors of the bubbles are characterized by the two ellipses with the semi-major/minor axis of 4/3 kpc, while parts of their outer edges are outlined for our spectral analysis of enhanced X-ray emission (see also Fig. 13). For comparison, these outlined regions are also shown in (C) the 3-color image obtained in the three HST filters (red - f814w, green - f555w, and blue - f438w) and (D) the GALEX FUV image of the galaxy.
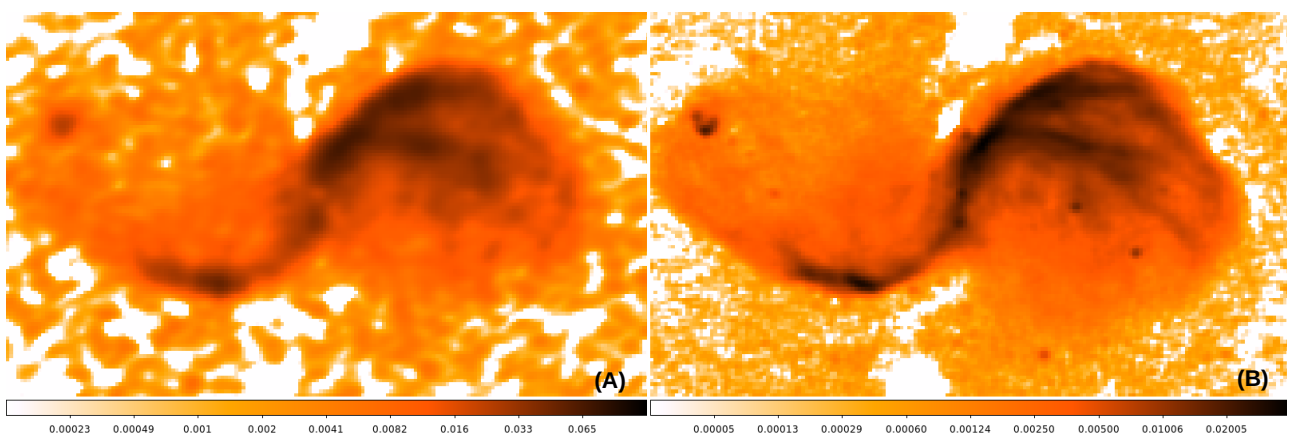
Figure 12: Same as Fig. 11A and B, but with the disk contributions approximately subtracted. Unit in Jy/Beam

We use the broad-band count and exposure maps to detect discrete sources using the WAVEDETECT

Table 2: Chandra Observation details of M106

Obs_ID	Cleaned Exposure	Mode	Dates
	ks		
350	14.04	FAINT	2000-04-17
1618	20.92	VFAINT	2001-05-28

tool at scales of 1.0, 1.4, 2.0, 2.8, 4.0, 5.7, and 8.0 pixels. The detected sources are shown in Fig. 13B. The data within 1.2 times the 90% energy-encircled region (EER) of each source are excluded in our analysis of the diffuse X-ray emission of the galaxy.
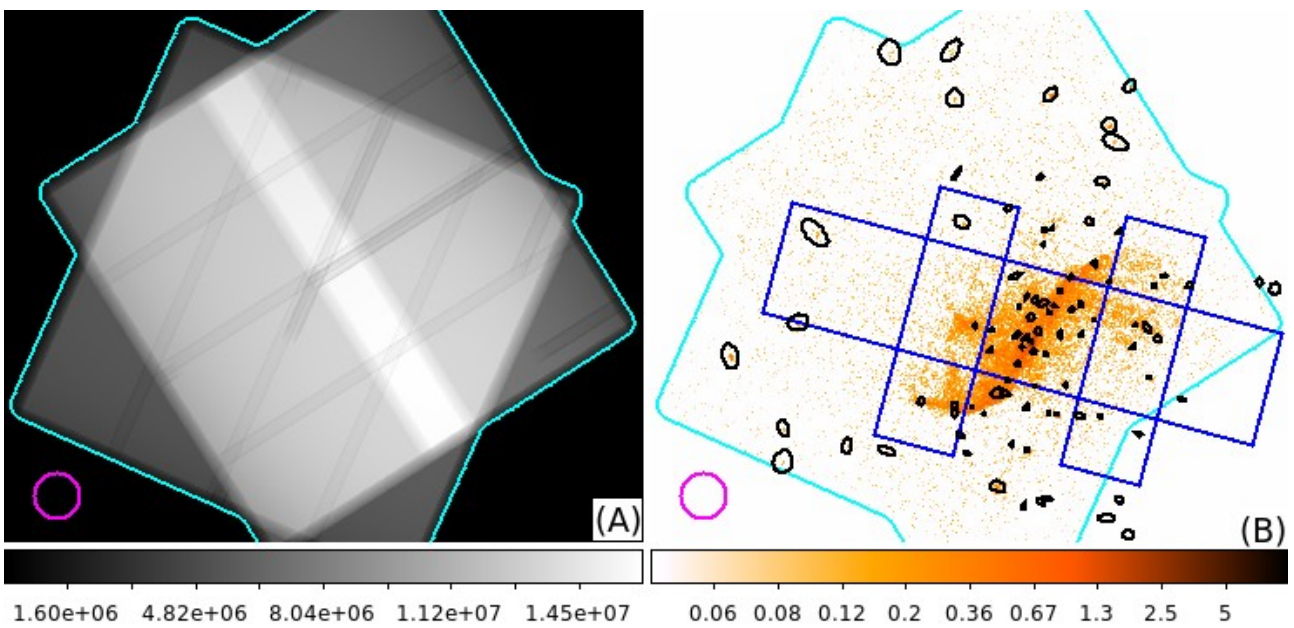
Figure 13: Overview of the Chandra data used in the present study of M106: (A) the effective exposure map (in units of s cm^2) constructed in the 0.45-1 keV band; (B) the 0. 5-7 keV count map, together with the black ellipses enclosing the 90% EER regions of individual detected sources and the boxes outlining the regions used to construct the 1-D radio/X-ray intensity distributions shown in Fig 20 (the regions parallel and perpendicular to the galaxy's minor axis have dimensions of 5.5 kpc × 23.7 kpc and 3.6 kpc × 11.5 kpc, respectively). In both panels, the field covered by the data is outlined by the cyan contour at the effective exposure of 1×10^6 s cm^2, while the magenta circle in the lower left corner illustrates the 1 kpc radius at the distance of the galaxy.

For this analysis we also need to consider the contributions from both non-X-ray events and the local sky X-ray background. The latter component is estimated from a spectrum extracted from a rectangular region northeast of M106, labeled "BKG" in Fig. 14 (This is also used for other wavelength local sky background), while the former is estimated from the data taken when the telescope was stowed out of the focal plane and under the shield[2]. We select the stowed data taken on the dates closest to the epoch of the M106 observations and reprocess them to match the observations in terms of both roll angles and count rates detected in the 10-12 keV band, where little X-ray contribution

---

[2]http://cxc.harvard.edu/contrib/maxim/stowed/

is expected. We subtract the resulting non-X-ray event component from the subsequent imaging and spectroscopic analyses.

2.2.2 Spatial Analysis

In addition to mapping the X-ray emission in the different bands, we also produce 1-D plots that provide a more quantitative assessment of the intensity distributions and comparison with multi-wavelength data. Specifically, these plots are generated in the three rectangular regions outlined in Fig. 13. We adaptively divide the parallel region (relative to the galaxy's minor axis) into vertical slices roughly from east to west, each containing a similar number of counts (~ 100). Similar divisions are made in the two vertical regions. For comparison, we use the same divisions to calculate the radio intensity distributions with the LoFAR data.

2.2.3 Spectral Analysis

Our spectral analysis of the diffuse X-ray emission uses XSPEC, which is part of the HEASOFT v6.31 software suite. We first characterize the local sky X-ray background spectrum after subtracting the non-X-ray contribution. While the procedure is detailed in the Appendix A, we find the best-fit model characterization satisfactory and thus use it to predict the X-ray background contributions in different on-source regions (Fig. 14), taking into account the differences in sky coverage and effective exposure. The non-X-ray and local sky X-ray contributions are combined and then subtracted from an on-source spectrum before further analysis.

Our on-source spectral analysis aims to provide a simple characterization of the thermal and chemical properties of the diffuse hot plasma associated with the bipolar superbubble structure of M106. We extract spectral data not only from the two entire bubbles, but also separately from their interiors and from the bright edge regions, as shown in Fig. 14. To allow differential spectral analysis of the bubble interiors, we further divide them into segments, E1-E3 and W1-W3 (Fig. 14). The sizes of these segments are adjusted so that they contain a similar number of counts (~ 1700 for the eastern division and 1250 for the western division) in the 0.45-1 keV band. The spectra from the entire bubbles or the interiors are adaptively grouped to ensure an S/N > 3 per bin, where S is the net number of counts after background subtraction, while N is the Poisson error of the total on-source counts of the bin. The other spectra (from the individual segments or edges) are binned to have S/N > 2.

The limited count statistics and spectral resolution of the spectral data allow only relatively simple modeling. However, we find that an optically thin one-temperature (1-T) thermal plasma (APEC) is far from being statistically acceptable (e.g., Table 3). Physically, the study based on the cosmological simulations (e.g., Pillepich et al., 2021, and discussion in § 4.4) shows that the temperature within such bubbles is widely distributed, e.g., ranging from several 10^6 K (typically found at the outer boundary) to $\gtrsim 10^7$ K (in the interior near galactic centers). In comparison, the variation of the plasma thermal pressure is relatively small (e.g. typically $<$ a factor of 2, probably except for regions near galactic disks), apparently due to the short dynamic (or sound-crossing) time scale of the hot plasma. The X-ray emission measure (EM) of the plasma is thus approximately $\propto n_e n_H \propto T^{-2}$ (see further discussion in § 4.1). Accordingly, we adopt a simple plasma model with a lognormal temperature distribution VLNTD (Cheng et al., 2021; Wang et al., 2021), which has the key parameters
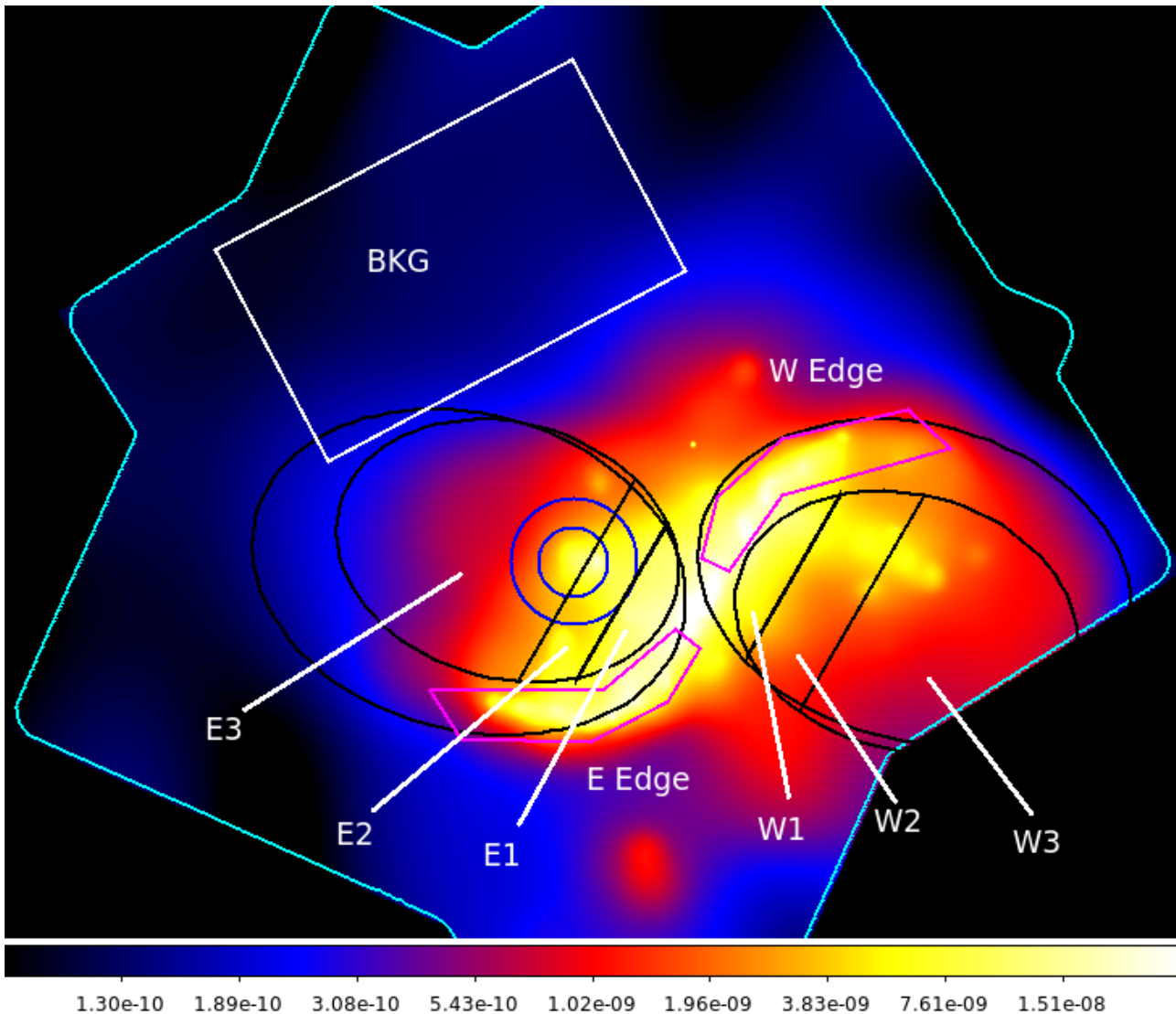
Figure 14: Diffuse X-ray emission map of M106 Units in Counts/s/cm^2. This map is constructed in the 0.45-1 keV band after removal of detected sources and smoothed with the CIAO routine csmooth with S/N >3. Several spectral extraction regions are outlined: the two large ellipses for the entire E and W bubbles, as well as their (E and W) interiors (represented by the two smaller ellipses) and (E and W) edges, which are the same as in Fig. 11. Segments of the bubble interiors and the background field (BKG) of the bubbles (same as in Fig. 10) are also marked. In addition, the small blue circle inside the E bubble encloses a hot spot with respect to its local background estimated in the annulus defined by the two blue circles. The cyan contour is the same as in Fig. 13.

as $\bar{x} = \ln(\bar{T})$ and σ_x – the emission-weighted mean and dispersion of the temperature in logarithmic form. Other parameters such as metal abundances and normalization are the same as in the VAPEC model.[3] The suitability of using the lognormal temperature distribution to describe the thermal properties of the hot CGM has also been recently demonstrated by Vijayan & Li (2022).

---

[3]https://heasarc.gsfc.nasa.gov/xanadu/xspec/manual/node134.html

In any case, we find empirically that this plasma model plus a foreground absorption or TBABS(VLNTD) gives a reasonably good characterization for most of our spectra.

3   Results

The presence of a prominent large-scale bipolar superbubble structure with enhanced diffuse radio emission is evident in Fig. 10. This structure is nearly perpendicular to the major axis of the galactic disk of M106 (including the two grand spiral arms, clearly visible in the 144 MHz band; see also Fig. 11). Fig. 9 presents a simplistic illustration of the major components of M106 that are most relevant here. The physical link of the bubbles to the disk and/or nucleus of the galaxy is not clear in the available data and will be discussed in § 4.4. Fig. 11 shows a close-up of the structure and a comparison with the multi-wavelength data of the galaxy. The diffuse radio emission associated with the structure is bounded on its southeastern and northwestern sides by the previously known east and west anomalous arms (Fig. 9), which are offset from the normal spiral arms seen in the HST or GALEX FUV images of the galaxy (Fig.11 C-D). Therefore, these two arms appear to represent parts of the outer boundaries of the bipolar super-bubble structure of the diffuse radio emission. There are other arm-like features (Fig. 11). While two of them are obviously the radio counterparts of the two normal grand spiral arms, the nature of the inner radio arm (marked in Fig. 9), which could be a separate outflow structure of the galaxy, is not clear. The total fluxes are 75/26 Jy at 54/144 MHz within the fields of the two ellipses (Bubbles) and 33/13 Jy within the two bright bubble edges (outlined regions in Fig. 11).

Figure 15 shows the radio spectral index map constructed from the LoFAR data. The spectral index is $\alpha \approx 1$, clearly indicating the synchrotron nature of the radio emission, and shows only a small region-to-region variation of typically $\lesssim 30\%$. Nevertheless, the spectral index appears systematically small along the southeast and northwest rims of the bubbles (Fig. 15A). This overall S-shaped substructure, including both the E and W edges or anomalous arms outlined in Fig. 11, may mark strong shock fronts where cosmic-ray acceleration is greatly enhanced. The average value is 0.92 ± 0.06 (0.27 RMS) in the E edge and 0.88 ± 0.04 (0.19 RMS) in the W edge, compared to 0.99 ± 0.02 (0.18 RMS) and 1.11 ± 0.02 (0.21 RMS) in the E and W bubble interiors. In each bubble interior, the spectral indices are 1.18 ± 0.09, 0.95 ± 0.06, and 1.08 ± 0.05 for regions E1-E3, and 1.19 ± 0.09, 1.14 ± 0.05, and 1.11 ± 0.03 for regions W1-W3 (Fig. 14). Thus, there is no clear trend for the spatial variation of the spectral index within the bubble interior, although the index tends to be smaller along the inner radio arm (Fig. 15B), probably marking local cosmic ray acceleration. We find that the inner radio arm, as well as the two anomalous arms or the bubble edges, stand out in the ratio map of the index to the 144 MHz intensity (Fig. 16), indicating that they are truly distinct from nominal galactic disk features such as regular spiral arms.   There is also an overall anti-correlation between the index and the intensity of the nonthermal radio emission in the bubbles (Fig. 15B). This is more quantitatively demonstrated in Fig. 17, where the data with (blue) and without (red) the disk subtraction are shown, as well as the mean index value (green) in the off-bubble galactic disk fields. The index value of the disk is smaller than those in the bubble fields, but is consistent with the value ~ 0.80 typically observed for the nonthermal radio emission in nearby disk galaxies (e..g, Basu et al., 2015). The galactic disk contaminates the bubble fields mostly near the major axis of the galaxy, where the bubble radio emission also tends to be strong. Fig. 17 shows that the subtraction of the disk contribution does not significantly change the results. So for simplicity, we keep using the radio data in the subsequent analysis without the disk subtraction. At the low intensity range of $\lesssim 0.005$ Jy beam^{-1}, the RMS in the index calculation is large, which may explain the lack of an apparent anti-correlation. An extrapolation of the overall index-intensity anti-correlation at the high intensity side toward even higher intensities would predict that the index could be considerably smaller intrinsically at the rims, which
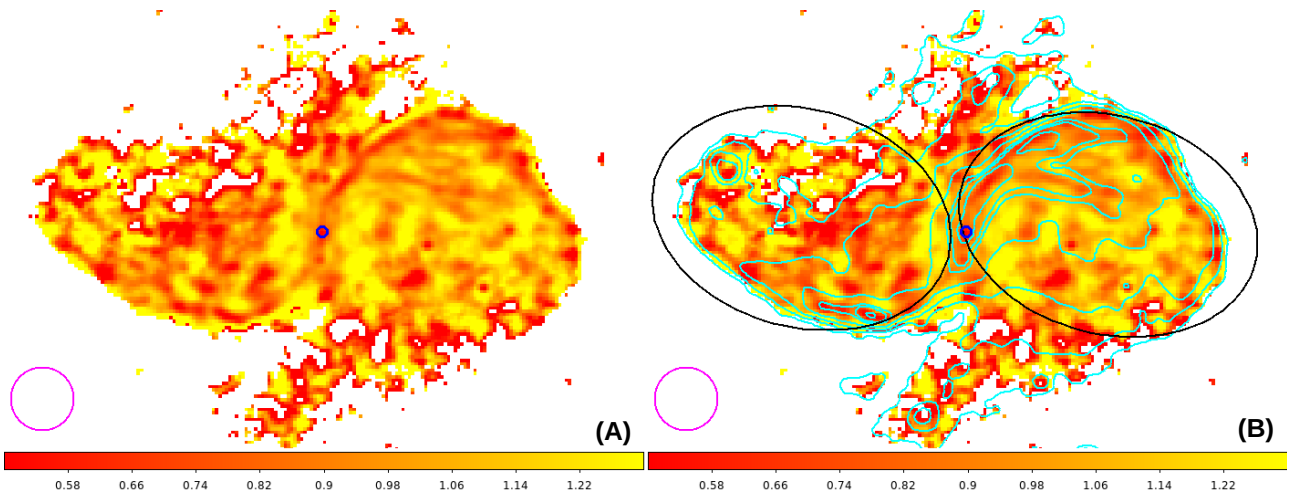
Figure 15: Radio spectral index map of M106 (panel A). The position of the galaxy's AGN is marked by the blue circle, while the radius of the magenta circle at the lower left corner indicates the 1 kpc scale. In panel B, the same index map is compared with the LoFAR 144 MHz intensity illustrated by the cyan contours at (0.07, 0.15, 0.3, 0.6, 1.2, 1.5, 2.2, 3, 6, and 9) $\times 10^{-2}$ Jy beam^{-1}. The two large ellipses mark the bubbles as in Fig. 14.
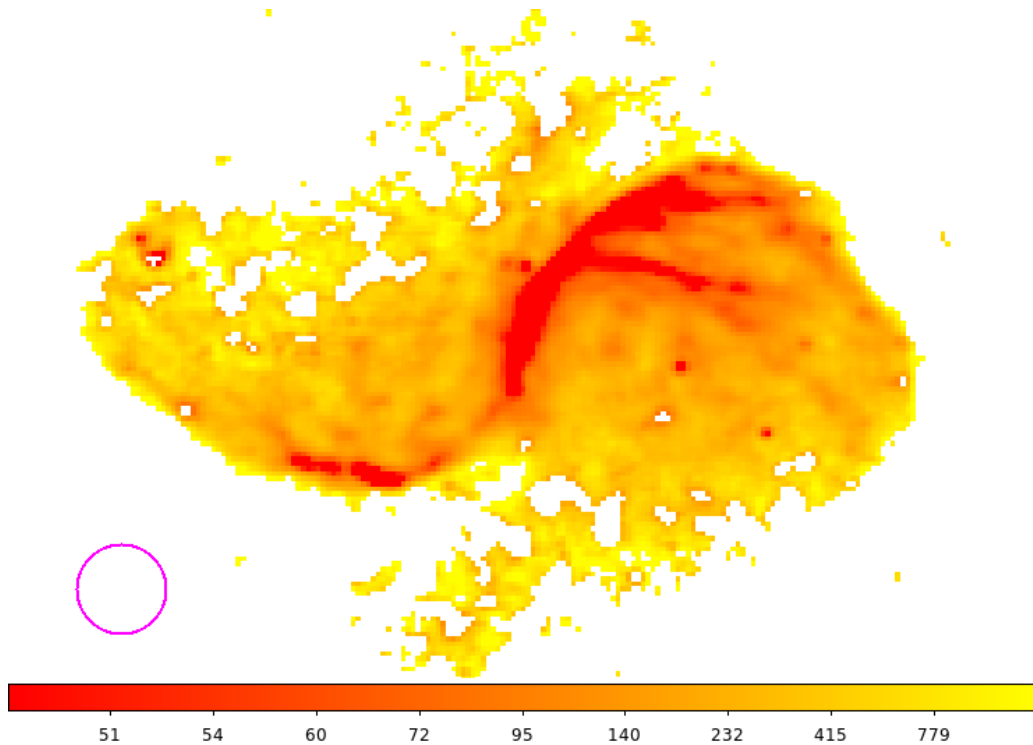
Figure 16: Ratio map of the radio spectral index to the 144 MHz intensity in units of $15''$ beam Jy^{-1}. The blank (or white-colored) regions are either due to index values < 0.3 or not included in the index calculation (§ 2.1).

are not well resolved in the LoFAR data. Indeed, based on the high spatial resolution VLA data at 6 cm and 20 cm Hyman et al. (2001) show that the brightest ridges of the rims or the anomalous arms have the index of 0.65 ± 0.1. We will explore the implications of the index-intensity anti-correlation in § 4.2.
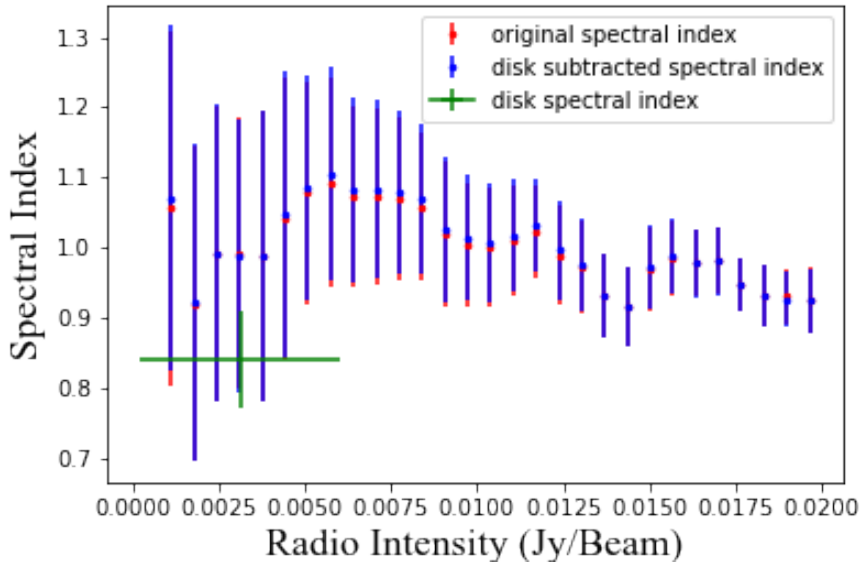
Figure 17: Radio spectral index vs. 144 MHz intensity in the bubble regions, as outlined by the two large ellipses in Fig. 15B. The index is calculated before (red) or after (blue) subtraction of the disk contributions in the two LoFAR bands (§ 2.1), while the horizontal axis is for the same 144 MHz intensity before the subtraction. The error bars represent the RMS of the spectral index data in each bin.

The radio bubbles are also visible in the X-ray images (Figs. 14, 18 and 19). The X-ray enhancement, most pronounced in the 0.45-1 and 1-2 keV bands, traces hot plasma emission, in contrast to the 2-7 keV band, which is dominated by point-like sources. In Fig. 18, the large-scale orange-colored diffuse emission off the central galactic disk has an overall morphology similar to the radio bubbles and their rim-brightened edges (see also Fig. 19), while green or white dots represent point-like sources that are excluded from the analysis of the diffuse X-ray emission (e.g. Fig. 14). This similarity is most striking for the W bubble (Fig. 19) with comparable total off-disk extents. For the E bubble, however, the diffuse X-ray emission is enhanced near the galactic disk and drops off steeply beyond about half the LoFAR bubble extent. The limited counting statistics of the X-ray data prevent us from a detailed 2-D study of the diffuse X-ray emission substructure. Part of this enhancement is due to a feature that we refer to as the eastern "hot spot" in Fig. 14. This X-ray feature, however, has no apparent multi-wavelength counterpart.

Fig. 20 presents the intensity distributions across the three rectangular cuts shown in Fig. 13. We use these distributions to examine the overall dimensions of the two bubbles. The (mostly east-west) distribution parallel to the minor axis of the galaxy (Fig. 20A) shows that the radio intensity drops sharply at ~ 8 kpc away from the center of M106, which can be considered as the total extent of the bubbles above and below the galactic disk; the projection correction for the disk inclination of $71°$ is only 6%, well within our estimation uncertainty. The X-ray intensity generally is expected to decrease faster than the radio emission, because the former (assumed to be thermal; see below) is
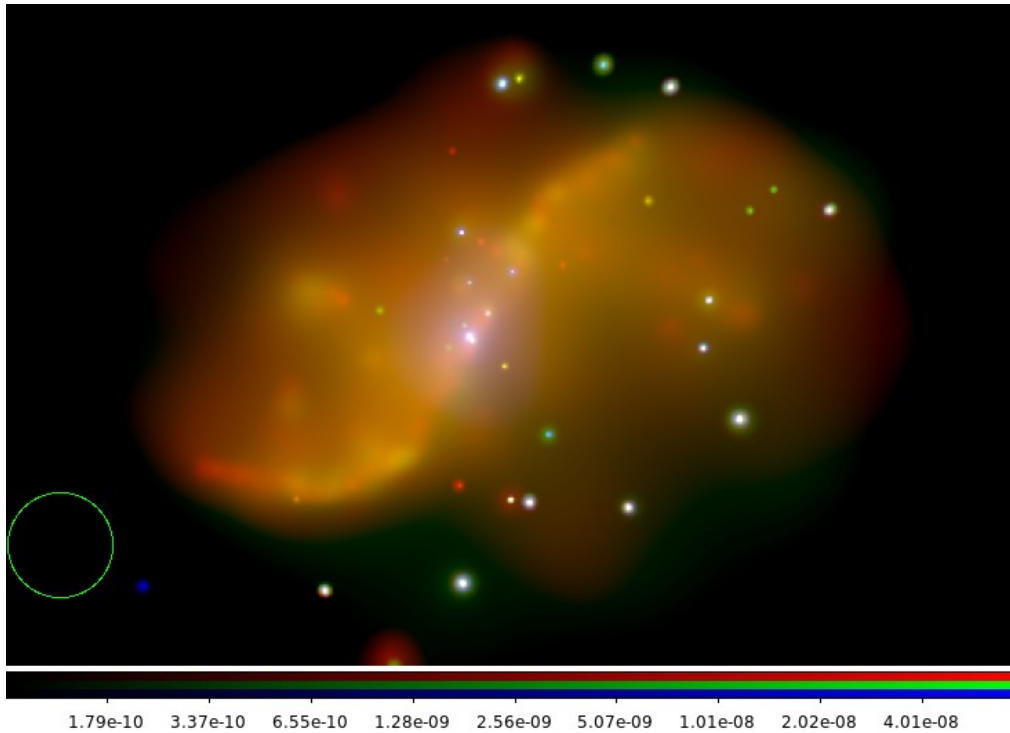
Figure 18: 3-color composite of the intensity images of M106 in the 0.45-1 keV (red), 1-2 keV (green), and 2-7 keV (blue) bands. These images have been smoothed with the CIAO CSMOOTH routine to achieve S/N > 3. The radius of the green circle at the lower left corner illustrates the 1 kpc scale.

more sensitive to density than the latter. Within 3 kpc of the major axis of the disk, the X-ray intensity is typically higher on the eastern side than on the western side, which is at least partly due to the absorption effect of the galactic disk. In addition, the distribution shows a shoulder at about 6 kpc on both sides. This shoulder may represent an outer shell-like feature of the bipolar structure, but this needs to be confirmed with better X-ray data. The cuts vertical to the minor axis of the galaxy (Fig. 20B-C) show the central X-ray enhancements as well as a separate peak about 4 kpc south of the E bubble center or 3 kpc north of the W bubble center, corresponding to their rim-brightened edges. However, the edge brightening is not apparent on the other sides of the bubbles. Nevertheless, a steep radio/X-ray intensity drop is seen at $\sim 2 - 3$ kpc off-center distances, north and south for the E and W bubbles, respectively. The enhancements near the minor axis of the galaxy are largely due to discrete features: the X-ray hot spot in the east and the inner radio arm in the west (Figs. 9, 14 and 19). Fig. 21 shows the X-ray spectra of the two bubbles. Due to the overall steep shape, as well as apparent emission line features that can be identified as being due to transitions such as Ne, Mg, and Si He-α, the spectra must be primarily thermal. Table 3 presents our spectral fit results based on the 1- or 2-T APEC plasma modeling, chiefly for comparison with previous similar studies (see § 4.3). We present our results mainly from the TBABS(VLNTD) modeling (Tables 4), which is more physically realistic.

Our spectral analysis shows that the foreground absorption is consistent with the hypothesis that the E bubble is on the near side of the galactic disk (e.g., Table 3; Fig. 9). Therefore, we fix the absorption to the known Galactic HI column density $N_{\mathrm{H,G}}$ (Table 1). In contrast, the fitted $\mathrm{N_H} \approx 2.3 \times 10^{21}$ cm^{-2}
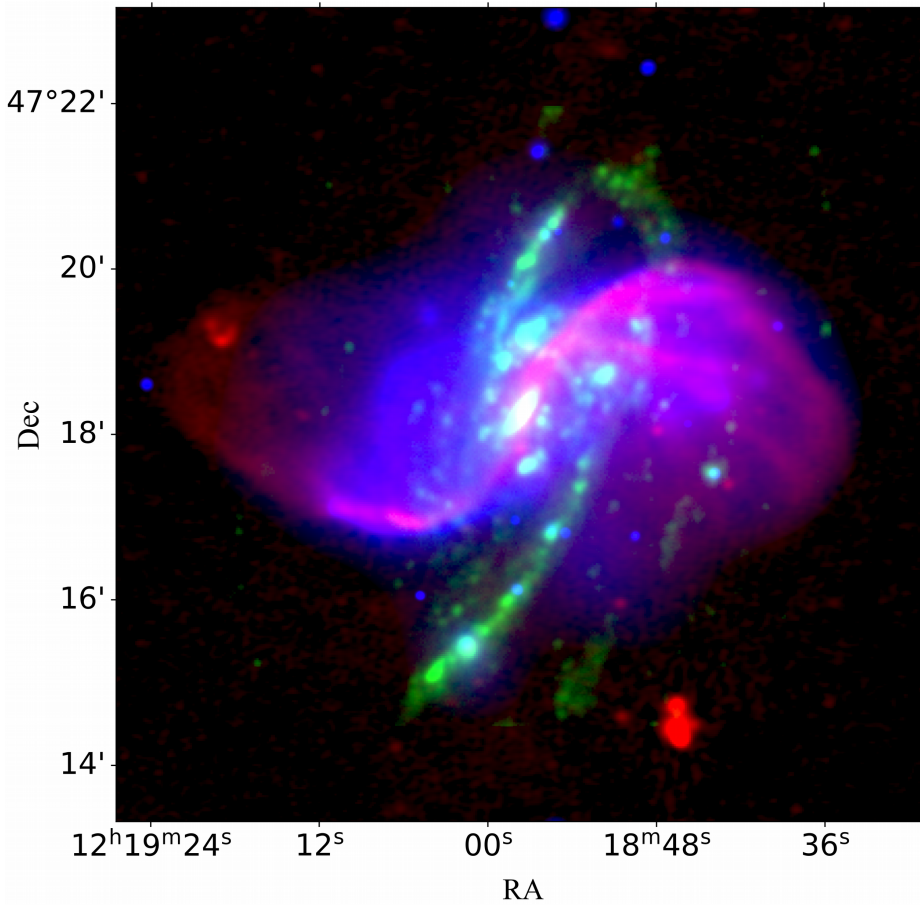
Figure 19: 3-color composite of the intensity images of M106 in the LoFAR 144 MHz (red), GALEX FUV (green), and Chandra 0.45-1 keV (blue) bands.

for the W bubble is larger than $N_{H,G}$, consistent with its location on the far side of the galaxy and its emission going through the disk. We find that both the mean temperature and the X-ray luminosity of the plasma in the W bubble are consistently higher than in the E bubble. The different spectral models give very different values for the metal abundance (Z) of the plasma (Table 4). The value increases from 1-T APEC, to 2-T APEC , and to VLNTD, reflecting their increasing proximity to the real temperature distribution of the plasma. However, in the VLNTD model, Z is strongly correlated with σ_x (Fig. 22), leading to the larger fitting errors reported for these parameters in Table 4.

Although the TBABS(VLNTD) modeling of the entire bubbles gives a reasonable characterization of their overall X-ray spectral shapes, the fits are having large reduced χ^2.

We thus further present the results of the TBABS(VLNTD) model fitting to spectra extracted from the sub-regions of the bubbles. Fig. 23 presents the fits to the data from the E and W bubble interiors, which cannot be rejected at the statistical confidence $\gtrsim 3\sigma$ (Fig. 14; Table 4). Even better fits are obtained for the spectra from the individual segments of the bubble interiors (Fig. 14; Table 4). The best-fit mean temperature seems to decrease with increasing distance from the galaxy's major axis, i.e. from E1 to E3 and from W1 to W3. However, the temperature dispersion (σ_x) shows an opposite trend, increasing with distance, because the two parameters are statistically anti-correlated in the spectral fits. To minimize this degeneracy effect and to check how the mean temperature might
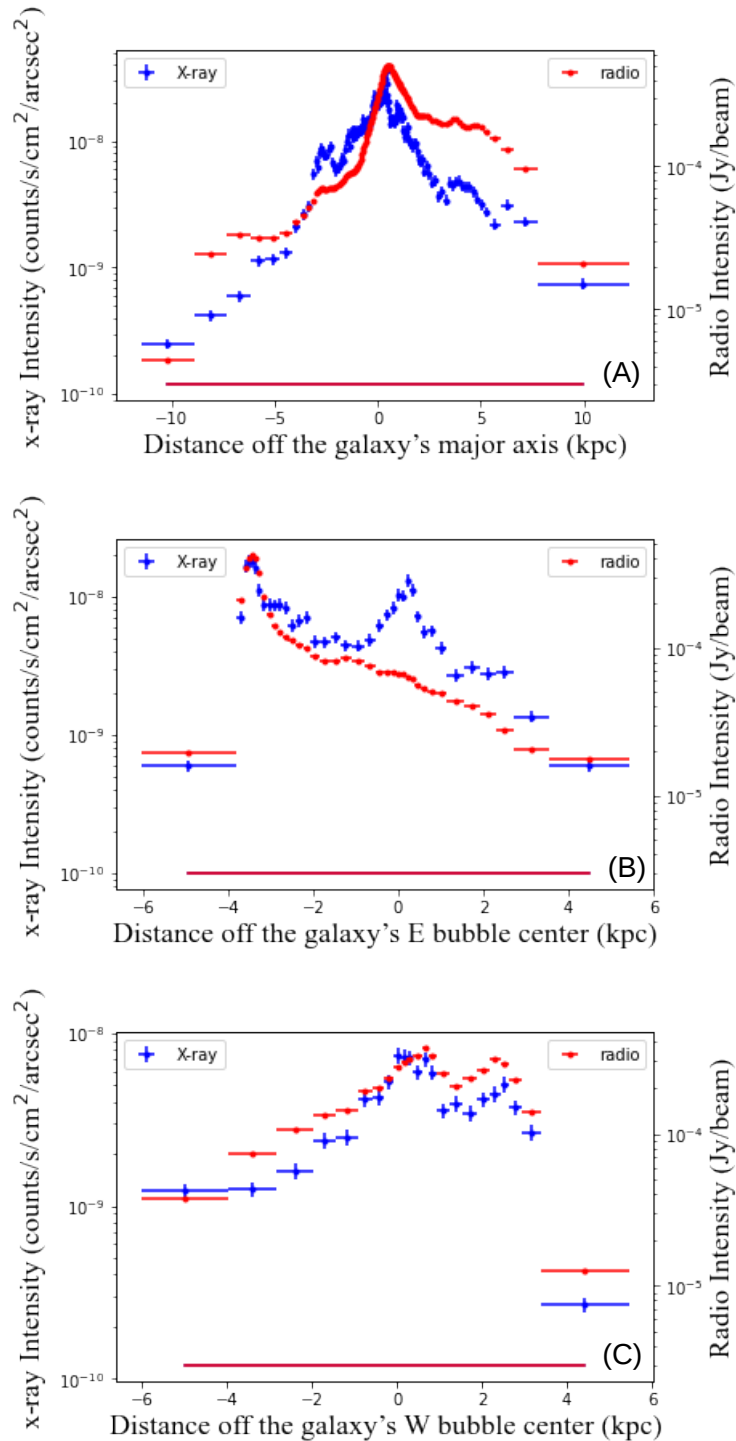
Figure 20: 1-D intensity profiles along the cuts shown in Fig. 13: LoFAR 144 MHz (red) and the 0.45-1 keV diffuse emission (blue). The parallel plot (A) has its coordinate centered on the major axis of the galaxy (positive toward the southwest), while the vertical plots (B - east cut; C - west cut) are centered on the ellipse centers of the bubbles (positive toward the northwest). The straight horizontal lines mark the local radio and X-ray background levels (Overlapped so only Radio shown). The positive offsets of the data points above the levels are due to the presence of the radio/X-ray-emitting CGM even outside the bubbles.
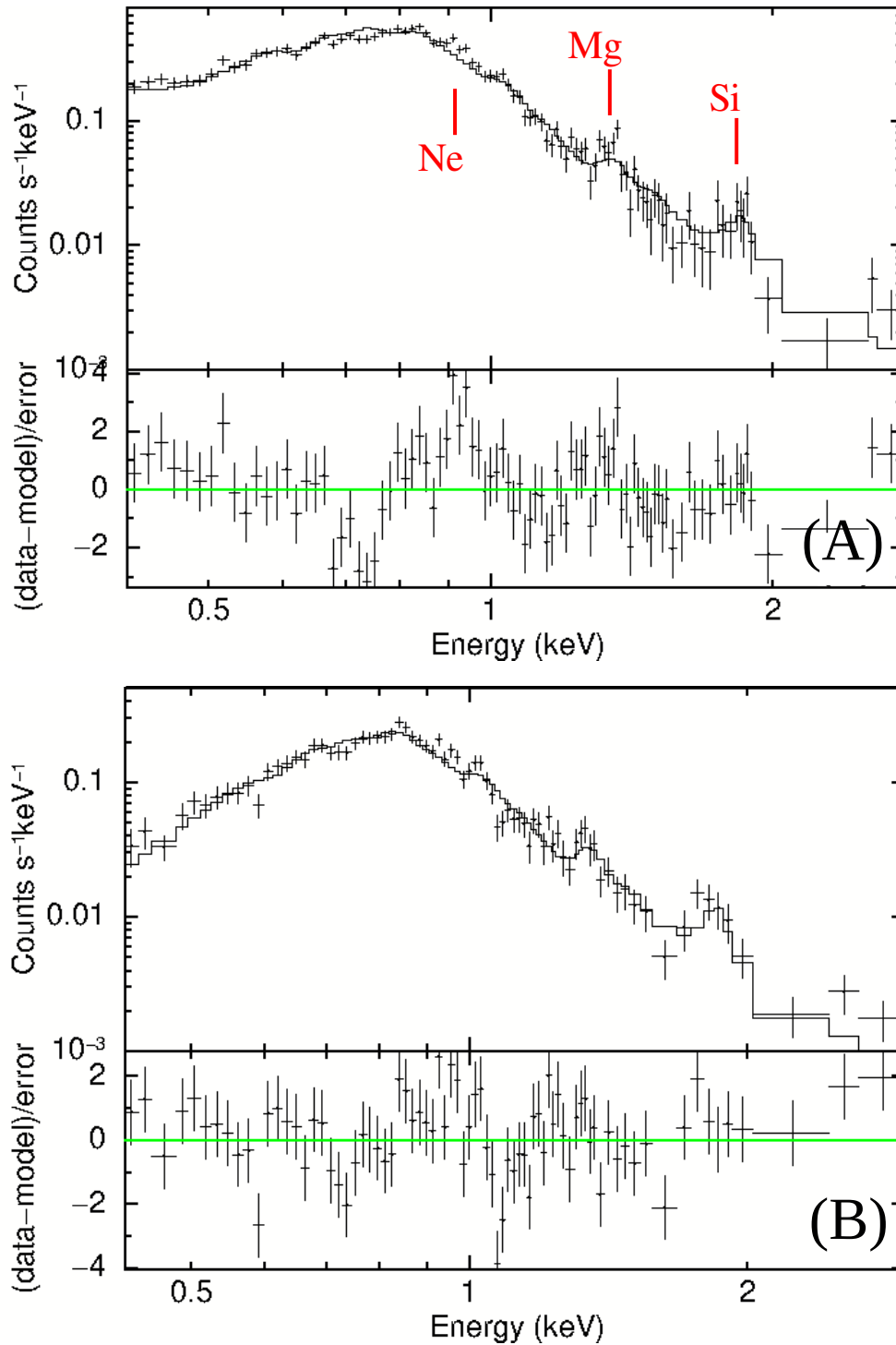
Figure 21: X-ray spectra of the E and W bubbles (A and B panels; Fig.   14), together with the best-fit TBABS(VLNTD) models (Table 4). These fits are not satisfactory, especially to some of the prominent He-α transitions expected for the thermal emission, which are marked in (A) for reference.
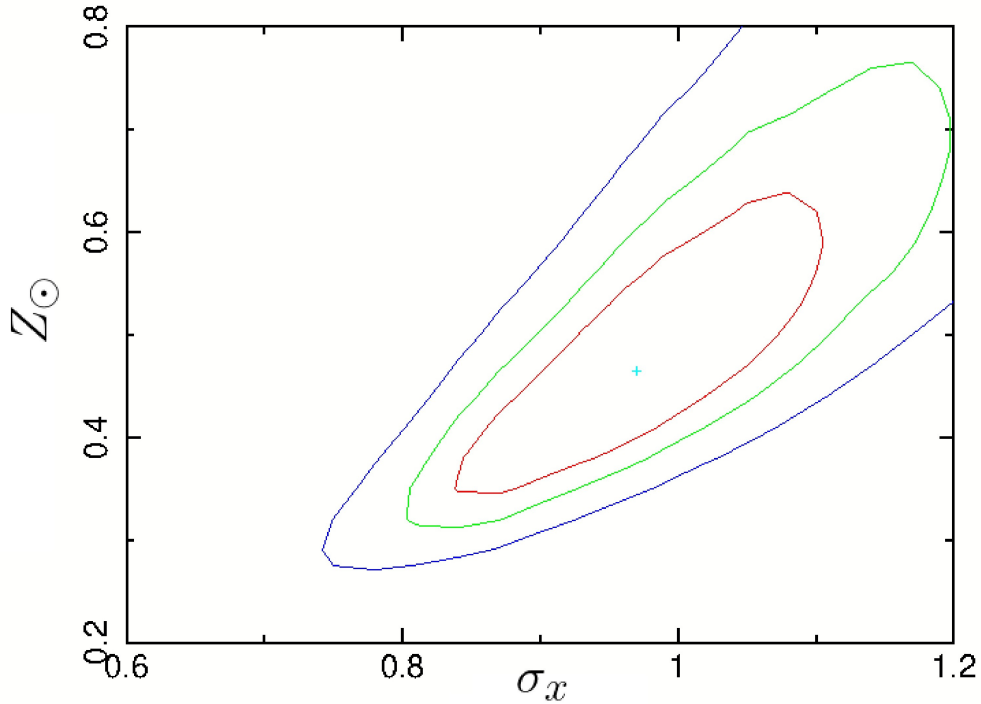
Figure 22: Illustration of the anti-correlation between the metal abundance Z and the lognormal temperature dispersion σ_x in the TBABS(VLNTD) model fit to the spectrum of the E bubble (Fig. 21). The confidence contours are at 68.3%, 95.4%, and 99.7% around the best-fit, marked as the plus sign (Table 4).

vary between the segments, we perform a joint fit of the E1-E3 and W1-W3 spectra (Figs 24) with the common fitting temperature dispersion σ_x and with both the metal abundance and the absorption column fixed at the best-fit values for the E and W interiors (Table 4). The fitted parameters are listed in Table5. While the quality of the fit does not change much (as judged by the χ^2/dof values), the trend of decreasing mean temperature with distance disappears for both bubbles. Interestingly, the E bubble has both a higher mean temperature and σ_x than the W bubble when the abundance and absorption column are fixed. Also, we have fitted the W inner arm to compare with the W edge to understand its property. We found a slightly higher mean temperature and sigma of dispersion for the W inner arm compared to the W edge.

A similar joint fit also shows that the hot spot (Fig. 14) does indeed have a slightly higher mean temperature than its immediate surroundings in the E bubble field.
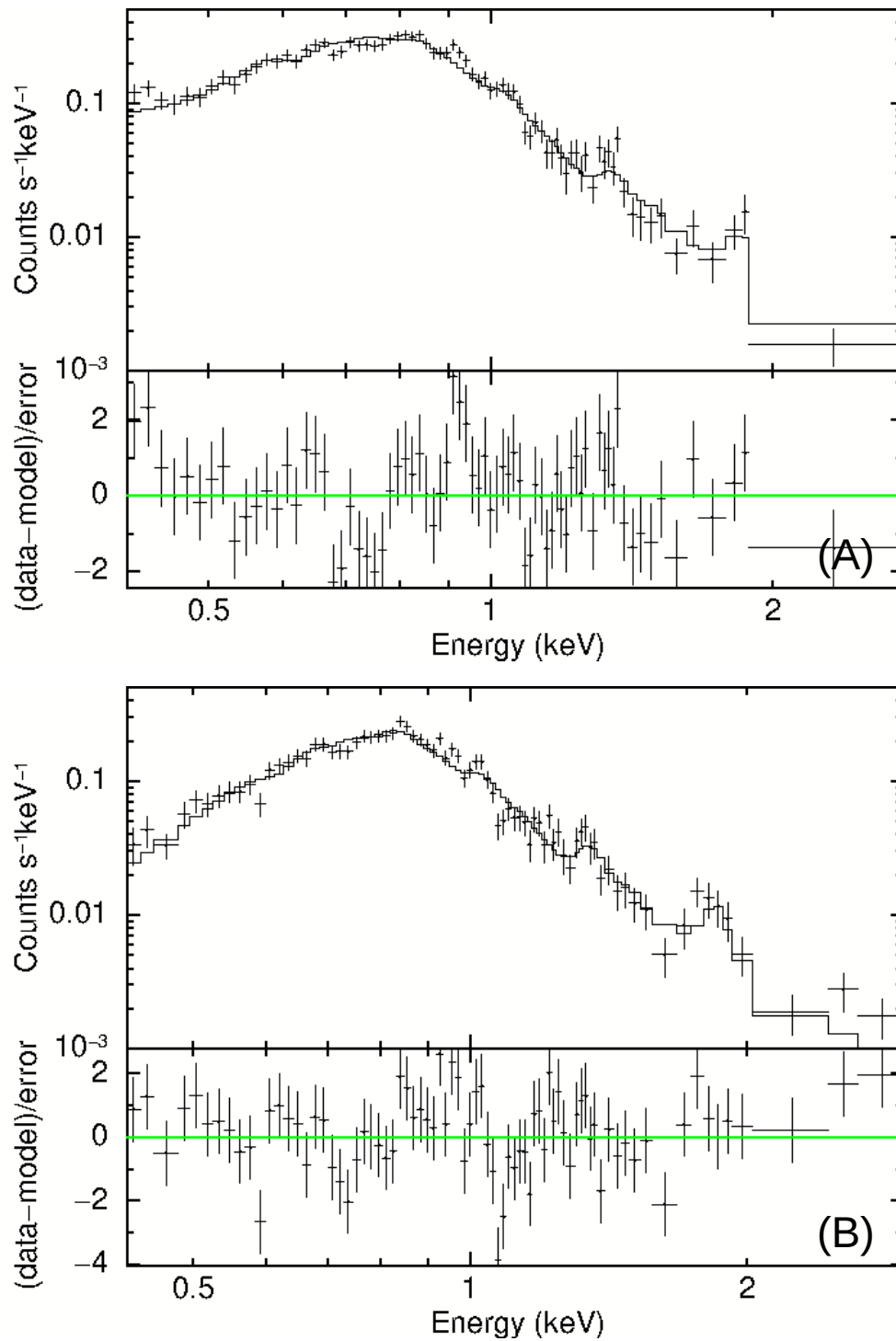
Figure 23: X-ray spectra of the E and W interiors (A and B panels; Fig. 14), together with the best-fit TBABS(VLNTD) models (Table 4).
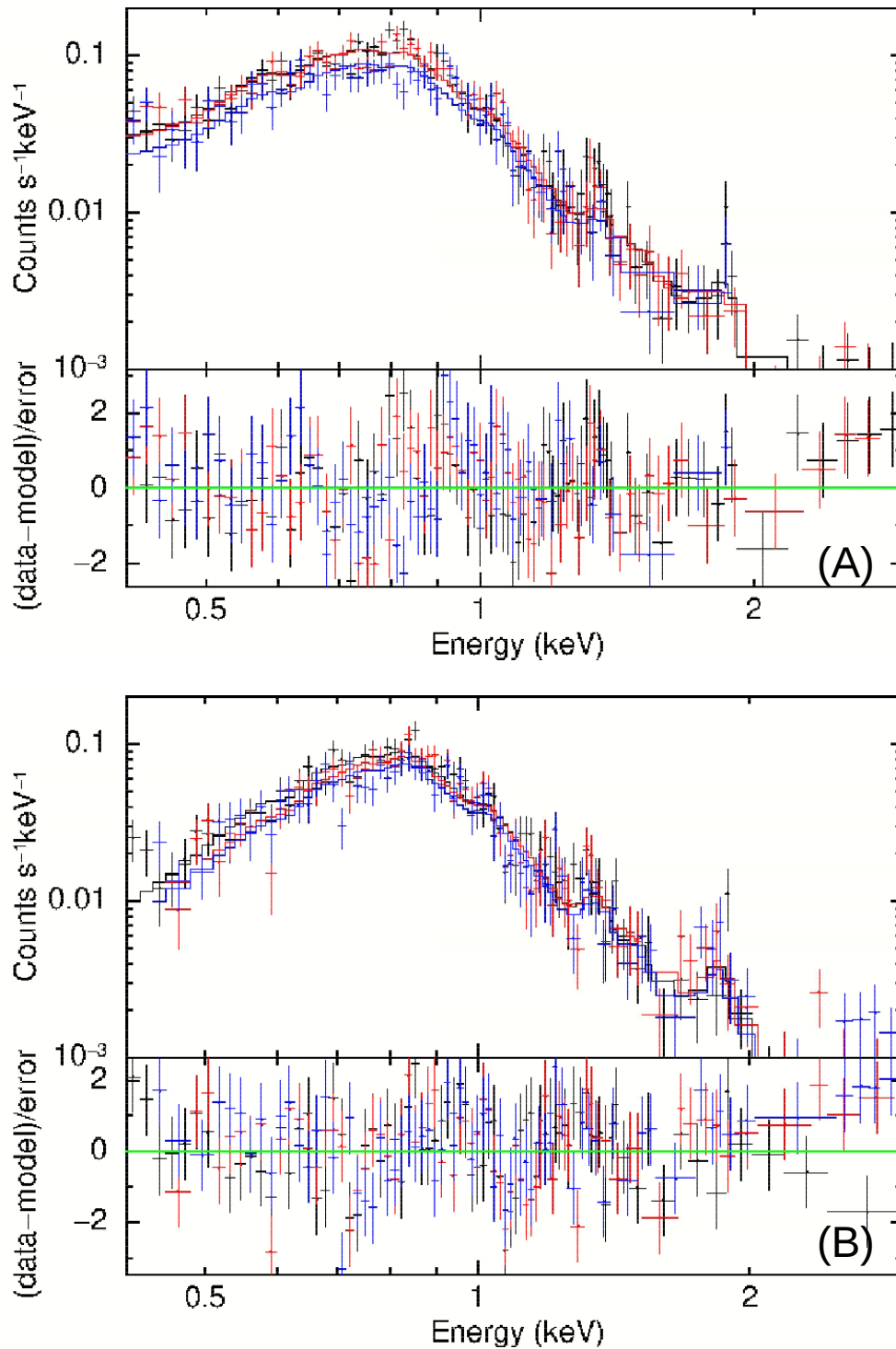
Figure 24: Joint TBABS(VLNTD) model fits to X-ray spectra extracted from the segments of the E and W interiors (Fig. 14), separately: (A) the east segment set [E1 (black), E2 (red), and E3 (blue)] and (B) the west segment set [W1 (black), W2 (red), and W3 (blue). For each segment set, both the fixed absorption and metal abundance, as well as the jointly fitted temperature dispersion and individually fitted mean temperatures are given in Table 5 (see text for details).

Table 3: 1-T and 2-T plasma model fit results

Region	area	nH	$k_B T_1$	$k_B T_2$	Z	K_{th1}	K_{th2}	χ^2/dof	f_x	L_x
	arcsec^2	10^{20}cm^{-2}	keV	keV	$Z_\odot$	10^{-3}cm^{-5}	10^{-3}cm^{-5}		10^{-13}erg cm^{-2}s^{-1}	10^{39}erg s^{-1}
E Bubble	43686	$0^{<8.22}$	$0.53^{+0.03}_{-0.01}$		$0.07^{+0.01}_{-0.01}$	$1.65^{+0.08}_{-0.10}$		422/92	5.69	6.30
-	-	$0^{<0.89}$	$0.24^{+0.02}_{-0.01}$	$0.76^{+0.03}_{-0.02}$	$0.26^{+0.05}_{-0.04}$	$0.58^{+0.10}_{-0.07}$	$0.46^{+0.08}_{-0.07}$	110/90	6.18	6.48
W Bubble	43686	$1.58^{+1.31}_{-1.09}$	$0.69^{+0.02}_{-0.02}$		$0.11^{+0.01}_{-0.01}$	$1.39^{+0.13}_{-0.13}$		344/127	5.80	7.20
-	-	$10.4^{+0.23}_{-0.21}$	$0.25^{+0.03}_{-0.02}$	$0.76^{+0.04}_{-0.03}$	$0.18^{+0.03}_{-0.03}$	$1.28^{+0.37}_{-0.31}$	$0.98^{+0.14}_{-0.15}$	188/125	6.06	11.1

Note: Listed parameters of the best-fit TBABS(APEC) (1st row) or TBABS(APEC$_1$+APEC$_2$) (2nd row) for each bubble: T_1 - the temperature of the APEC or APEC$_1$ plasma; T_2 - the temperature of the APEC$_2$ plasma; K_{th1} and K_{th2} - the corresponding normalizations of the two plasma components; χ^2/dof where dof is the degree of freedom of each fit. Also listed are the derived parameters: f_x - the absorbed flux in the 0.45-1 keV range and L_x - the (unabsorbed) 0.1-10 keV luminosity. All error bars are measured at the 90% confidence level.

Table 4: lognormal temperature plasma model fit results

Region	Area	N_H	$k_B \bar{T}$	σ_x	Z	K_{th}	χ^2/dof	f_x	L_x
	arcsec^2	10^{20}cm^{-2}	keV		$Z_\odot$	10^{-3}cm^{-5}		10^{-13}erg cm^{-2}s^{-1}	10^{39}erg s^{-1}
E Bubble	43686	$0^{<1.14}$	$0.31^{+0.03}_{-0.01}$	$0.97^{+0.15}_{-0.06}$	$0.46^{+0.18}_{-0.13}$	$1.29^{+0.28}_{-0.23}$	165/91	6.02	6.52
E Interior	27737	4.21(fix)	$0.25^{+0.06}_{-0.08}$	$1.02^{+0.31}_{-0.20}$	$0.42^{+0.31}_{-0.15}$	$1.16^{+0.29}_{-0.16}$	101/76	3.52	4.72
E1	2237	4.21(fix)	$0.27^{+0.05}_{-0.06}$	$0.89^{+0.20}_{-0.15}$	0.42(fix)	$0.36^{+0.08}_{-0.05}$	88/82	1.22	1.61
E2	4250	4.21(fix)	$0.23^{+0.06}_{-0.08}$	$1.03^{+0.24}_{-0.17}$	0.42(fix)	$0.41^{+0.13}_{-0.06}$	77/73	1.20	1.63
E3	21249	4.21(fix)	$0.15^{+0.19}_{-0.11}$	$1.43^{+0.21}_{-0.14}$	0.42(fix)	$0.47^{+0.24}_{-0.23}$	70/59	0.99	1.45
E edge	4827	4.21(fix)	$0.21^{+0.04}_{-0.05}$	$1.01^{+0.16}_{-0.13}$	0.42(fix)	$0.81^{+0.17}_{-0.11}$	120/85	2.31	3.12
W Bubble	43686	$6.31^{+4.72}_{-2.24}$	$0.41^{+0.08}_{-013}$	$0.96^{+0.18}_{-0.15}$	$0.39^{+0.12}_{-0.11}$	$1.86^{+1.13}_{-0.39}$	206/126	5.89	9.25
W Interior	22969	$23.2^{+6.4}_{-5.4}$	$0.13^{+0.20}_{-0.13}$	$1.12^{+0.06}_{-0.05}$	$0.76^{+0.71}_{-0.27}$	$1.73^{+0.85}_{-0.80}$	112/74	2.16	7.7
W1	2842	23.2(fix)	$0.19^{+0.05}_{-0.08}$	$0.85^{+0.27}_{-0.16}$	0.76(fix)	$0.52^{+0.33}_{-0.11}$	85/77	0.87	3.03
W2	6264	23.2(fix)	$0.18^{+0.09}_{-0.09}$	$0.96^{+0.34}_{-0.25}$	0.76(fix)	$0.47^{+0.33}_{-0.15}$	86/70	0.77	2.67
W3	14697	23.2(fix)	$0.14^{+0.10}_{-0.14}$	$1.12^{+0.12}_{-0.10}$	0.76(fix)	$0.53^{+0.03}_{-0.03}$	86/69	0.70	2.50
W edge	4919	23.2(fix)	$0.13^{+0.05}_{-0.05}$	$0.93^{+0.04}_{-0.04}$	0.76(fix)	$1.88^{+0.07}_{-0.07}$	165/90	2.21	8.19
W inner arm	3589	23.2(fix)	$0.14^{+0.08}_{-0.14}$	$1.01^{+0.53}_{-0.25}$	0.76(fix)	$0.57^{+0.09}_{-0.19}$	80/71	0.75	1.8

Note: Same as the caption to Table 3, but for the TBABS(VLNTD) model in which the listed parameters are $\bar{T}$ - the mean temperature; σ_x - the dispersion of the temperature in logarithm, and K_{th} - the normalization of the plasma (Cheng et al., 2021; Wang et al., 2021).

Table 5: Joint fit results of the VLNTD model to bubble segment spectra

Region	$k_B \bar{T}$	σ_x	K_{th}	χ^2/dof	f_x	L_x
E 1	$0.22^{+0.04}_{-0.05}$	$1.04^{+0.15}_{-0.11}$	$0.42^{+0.08}_{-0.05}$	90/85	1.20	1.65
E 2	$0.23^{+0.04}_{-0.05}$	-	$0.41^{+0.08}_{-0.05}$	77/76	1.20	1.65
E 3	$0.24^{+0.07}_{-0.05}$	-	$0.35^{+0.06}_{-0.05}$	74/62	1.00	1.37
W 1	$0.17^{+0.05}_{-0.05}$	$0.88^{+0.15}_{-0.12}$	$0.96^{+0.32}_{-0.20}$	86/80	0.86	3.13
W 2	$0.20^{+0.05}_{-0.05}$	-	$0.72^{+0.26}_{-0.14}$	90/73	0.76	2.69
W 3	$0.19^{+0.05}_{-0.05}$	-	$0.71^{+0.25}_{-0.16}$	88/72	0.71	2.51

Table 6: Inferred plasma parameters in individual regions of the bubbles

Region	V_t	P_{th}	E_{th}	EM	Mt_c	
	kpc^3	$f_h^{-1/2}$ keV cm^{-3}	$10^{56} f_h^{1/2}$ erg/s	10^{62} cm^{-3}	$10^7 f_h^{1/2}$ M$_\odot$	$f_h^{1/2}$ Gyr
E 1	9	0.040	0.28	2.88	1.6	0.53
E 2	23	0.029	0.47	2.81	2.53	0.90
E 3	118	0.012	1.02	2.40	5.31	2.36
W 1	9	0.038	0.24	6.59	2.08	0.24
W 2	45	0.017	0.56	4.94	4.03	0.66
W 3	96	0.011	0.77	4.87	5.85	0.97

4   Discussion

The results in the above chapter now enable us to infer the thermal and nonthermal properties of the superbubble structure in M106 and to make comparisons with those similar features observed in other galaxies, especially the eROSITA/Fermi bubbles in our Galaxy, and with the relevant simulations (Pillepich et al., 2021). Our goal here is to achieve a better understanding of the formation and evolution of the structures and their potential impacts on the host galaxies.

4.1   Physical properties of the bubbles in M106

We here infer the physical properties of the diffuse hot plasma enclosed in the bubbles. This inference is based on the spectral fitting results listed in Table 5, as well as the relevant formulae obtained for the VLNTD (Cheng et al., 2021; Wang et al., 2021), which include the thermal pressure

$$
\begin{aligned}
P_{th} &= \sqrt{\frac{4\pi D^2 \eta^2 K_{th}}{10^{-14} V_t}} (k_B \bar{T}) e^{\sigma_x^2} \\
&\approx (1.74 \times 10^{33} \text{ keV cm}^{-3}) \sqrt{\frac{K_{th}}{V_t}} (k_B \bar{T})_{keV} e^{\sigma_x^2},
\end{aligned}
\tag{2}
$$

the total thermal energy $E_{th} = \frac{3}{2} P_{th} V_t$, the integrated emission measure

$$
EM = \left[\frac{P_{th}}{\eta k_B \bar{T}}\right]^2 V_t e^{-2\sigma_x^2},
\tag{3}
$$

and the total mass of the plasma

$$
M_{th} = \frac{P_{th} \mu m_p V_t}{k_B \bar{T}} e^{-\sigma_x^2/2},
\tag{4}
$$

where V_t, is expressed as a fraction of the total ellipsoidal volume of the bubble. The entire bubble has a volume of approximately 150 kpc^3. The inferred parameters are included in Table 6. Overall, there is a trend of decreasing thermal pressure with the increasing distance from the galactic center for both bubbles. We estimate the mass of the plasma in both bubbles to be approximately $10^8 M_\odot$ and we estimate the cooling timescale of the plasma in a region as $t_c \sim E_{th}/L_{bol}$, where the bolometric luminosity L_{bol} is approximated as the unabsorbed luminosity L_x integrated over the 0.1-10 keV range (Table. 5).

4.1.1   W inner arm

By analyzing the fitted spectra presented in Table 4, we observed that the W inner arm exhibits a slightly higher mean temperature and a greater dispersion compared to the W edge. This disparity can be attributed to their respective connections: the W edge is linked to the AGN, while the W inner arm may be connected to the N hot spot, in the hypothesis that the AGN's jet has migrated from a different different to its present location. The W inner arm's delayed formation and higher temperature suggest a shorter cooling period. Therefore, we speculate that the W inner arm was formed at a later stage than the W edge, leading to its elevated temperature.

4.2   Nonthermal properties of the radio bubbles in M106

Here we first use our measurements of the radio emission to constrain the magnetic field in the bubbles, then explore the implications of the observed anticorrelation between the index and the intensity of the radio emission, and finally estimate the potential inverse Compton (IC) scattering contribution of cosmic ray electrons (including positions) to the diffuse X-ray emission.

We estimate the magnetic field strength, assuming the equipartition between the field and cosmic ray energy densities and following the equation (Beck & Krause, 2005):

$$
\begin{aligned}
B_{\mathrm{eq}} = \{ & 4\pi(2\alpha+1)(K_0+1)I_\nu E_P^{1-2\alpha}(\nu/2c_1)^\alpha \\
& /[(2a-1)c_2(\alpha)lc_4(i)] \}^{1/(\alpha+3)},
\end{aligned}
\tag{5}
$$

where E_P is the proton rest mass energy, the constants c_1, c_2, and c_4 can be found in Beck & Krause (2005), while $\alpha \approx 1$, as obtained above, i is the disk inclination (Table 1), and the constant ratio between the number densities of cosmic-ray protons and electrons $K_0 \sim 100$ is assumed, while I_ν is the surface brightness (e.g., in units of erg s^{-1} cm^{-2} Hz^{-1} sr^{-1}), which can be converted from our observed intensity at $\nu = 144$ MHz, and l is the path length along the line of sight of the radio-emitting region. The equation shows that the distribution of $B_{\mathrm{eq}}l^{1/4}$ is just a function of I_ν (e.g., Fig. 11B). It is clear that B_{eq} cannot be uniform in the bubbles. B_{eq} is about the smallest at the bubble centers where $l \sim 6$ kpc is the largest (if an ellipsoid is assumed) while I_ν is relatively small). For example, taking $I_\nu \sim 6 \times 10^{-4}$ Jy beam^{-1} at the east bubble center, we get $B_{\mathrm{eq}} \sim 3\,\mu\mathrm{G}$. The largest B_{eq} tends to be at the bubble edges. With $l \sim 0.3$ kpc, estimated as the full width of the half peak intensity (Fig. 20B), we estimate $B_{\mathrm{eq}} \sim 13\,\mu\mathrm{G}$ at the east edge. Similarly, we find $B_{\mathrm{eq}} \sim 4\,\mu\mathrm{G}$ and $\sim 13\,\mu\mathrm{G}$ at the west bubble center and edge. The corresponding magnetic field pressure is $\sim (0.6-4) \times 10^{-3}$ keV cm^{-3}, which is substantially smaller than the thermal pressure in the bubbles (e.g., Table 6), suggesting that they are primarily driven by the over-pressure of the hot plasma. However, the thermal pressure drops steeply with the increasing distance from the major axis of the galaxy (Table 6), while the decline of the radio intensity is much slower (e.g., Fig. 20A). Therefore, the magnetic field pressure becomes more important at the far ends of the bubbles.

What could be the cause of the anti-correlation between the spectral index and the intensity of the radio emission, as shown in Fig. 17? The most natural explanation is synchrotron steepening, as expected when cosmic ray electrons diffuse out of their accelerating regions with higher magnetic fields. Following (Murphy, 2009) and considering a critical frequency of $\nu_c = 144$ MHz, we estimate the cooling time scale as $t_{\mathrm{syn}} \sim (1.1 \times 10^8\ \mathrm{yr})(B/10\mu\mathrm{G})^{-3/2} \sim (0.8-7) \times 10^8$ yrs, assuming a field strength of $B_{\mathrm{eq}} \sim 3-13\,\mu\mathrm{G}$. If this assumption is reasonable, then the estimated t_{syn} puts a lower bound on the age of the M106 structure. Of course, if the actual magnetic field B is larger than the above B_{eq}, then this age limit should be correspondingly smaller. We could not find other similar plausible scenarios. For example, we do not expect significant thermal free-free absorption of the radio emission even at ~ 54 MHz in a galaxy like M106 (e.g., Israel & Mahoney, 1990; Basu et al., 2015). If this absorption were important, we would expect the index to be smaller on the W bubble side (behind the entire galactic disk) than on the E bubble side (in front of the disk). Ionization losses, which may be important in dense gas (e.g., Basu et al., 2015), can also be ruled out as an explanation for the anti-correlation, because of the relatively lower density environment of the M106 structure.

While we have so far assumed that the thermal plasma dominates the X-ray emission observed from the bubbles, it is important to check if the contribution from the IC scattering may be significant. In

or near the galactic disk of M106, seed photons of the process are expected to be produced primarily by interstellar dust, which peaks at $\sim 100\,\mu m$. The same electrons that upscatter such photons to X-rays should also produce the synchrotron emission in the MHz to tens of MHz frequency range (Cecil et al., 1995). Therefore, the low-frequency LoFAR data are well-suited to constrain the IC contribution, which we estimate, following the equation (Harris & Grindlay, 1979):

$$S_X = \frac{(5.05 \times 10^4)^\alpha C(\alpha) G(\alpha) (1+z)^{\alpha+3} S_r \nu_r^\alpha}{10^{47} B_{\mathrm{eq}}^{\alpha+1} \nu_X^\alpha}. \tag{6}$$

Adopting $C(\alpha) = 1.2 \times 10^{31}$ and $G(\alpha) = 0.5$ since $\alpha \approx 1$, as well as the redshift of the galaxy $z = 0.0016$, the intensity $S_r \sim 7.5$ Jy beam^{-1} at the frequency $\nu_r = 144$ MHz, $\nu_X = 1.2 \times 10^{17}$ Hz at 0.5 keV, and $B_{\mathrm{eq}} \sim 3\,\mu G$, we obtain $S_x \approx 3.3 \times 10^{-15}$, which is only $\sim 1\%$ of the total X-ray flux of the bubbles. Therefore, we conclude that the IC contribution to the X-ray emission is insignificant.

4.3 Comparison with other observations

We begin by comparing the M106 bubbles with the eROSITA/Fermi bubbles and Radio Loop I in our Galaxy. A major advantage of observing the bubbles in M106 is the minimal foreground confusion and extinction/absorption, especially towards its E bubble, which is in front of the inclined galactic disk. Indeed, our spectral analysis shows that there is little additional absorption towards the bubble beyond the Galactic one, while the absorption towards the W bubble is considerable ($N_H \sim 2 \times 10^{21}$ cm^{-2}), as expected from the disk.

Our X-ray spectral analysis shows a broad temperature distribution of the plasma in the M106 structure. Characterized by the Lognormal temperature distribution model, the bubble interiors consistently show $\sigma_x \approx 1$ and $\bar{T} \approx 0.2$ keV (Table 5). Of course, the quoted temperature characterization is model dependent. Thus, it is more appropriate to compare our alternative 1-T and 2-T plasma characterizations (Table 3) with results based on similar modeling for bubbles observed in other galaxies. Based on the 1-T plasma modeling, the mean temperatures of ≈ 0.53 and 0.69 keV for the E and W bubbles are substantially higher than 0.3 keV for the plasma associated with the eROSITA/Fermi bubbles (e.g., Ursino et al., 2016; Miller & Bregman, 2016; Kataoka et al., 2018). The thermal energy of the M106 structure is $\sim 3 \times 10^{56}$ erg (Table 6), which is comparable to the total energy estimated for the eROSITA/Fermi bubbles (e.g., Kataoka et al., 2018).

There are notable differences between the radio/X-ray enhanced edges of the M106 structure and the eROSITA/Fermi bubbles. The enhanced edges of the M106 structure exhibit an S-shape, which can be naturally explained by the tilted jets of the AGN (Wilson et al., 2001; Krause et al., 2007). In contrast, the eROSITA/Fermi bubbles is mainly enhanced on the Galactic northeast (positive Galactic longitude/latitude) side, which could be due to the ram pressure of a CGM wind from the Galactic northeast (Mou et al., 2023). Our estimated mean magnetic field strength ($\sim 13\,\mu G$) in the M106 edges is much greater than $\sim 4\,\mu G$ in the Radio Loop I around the eROSITA/Fermi bubbles Mou et al. (2022).

Now let us compare the M106 structure with the bubble northwest of the NGC 4438 nucleus. For this NGC 4438 nuclear bubble, both 2-T APEC (with $T_1 = 0.27$ keV and $T_2 = 1.2$ keV) and 1-T APEC ($T = 0.90$ keV) + power law have been considered, although the latter model is statistically favored (Li et al., 2022). The 2-T plasma characterization suggests that the plasma in the NGC 4438

bubble is considerably hotter than in the M106 E and W bubbles ($T_1 = 0.24$ keV and $T_2 = 0.76$ keV). Incidentally, there is an X-ray faint counter-nuclear bubble of a similar extent on the other side of the galactic disk of NGC 4438. The X-ray faintness of this bubble is largely due to the absorption of the inclined disk - a more extreme case than the W-bubble of M106. Both nuclear bubbles of NGC 4438 are associated with enhanced radio emission with a projected width of $\sim 3''$, which is not well resolved by the existing radio data (Li et al., 2022). In contrast, the radio morphology of the M106 bubbles is well resolved.

In addition to the previously detected bubbles in the Milky Way and NGC 4438, there have been other noteworthy bubble discoveries, such as the ones found in NGC 3079, measuring approximately 1.1 kiloparsecs in size (Veilleux et al., 1994; Li et al., 2019). However, these bubbles differ in several significant aspects from those observed in the eROSITA/Fermi bubbles or NGC 4438. Firstly, their initial detection was limited to the X-ray hard band, suggesting a non-thermal emission nature and ruling out the presence of a high-temperature thermal component. Moreover, the radio spectral index associated with these bubbles is notably larger, measuring 1.11 ± 0.34. Additionally, unlike the relatively symmetrical bubbles observed in our case or the eROSITA/Fermi bubbles and those in NGC 4438, the bubbles in NGC 3079 exhibit an asymmetric morphology in hard X-ray observations. The origin of the X-ray bubbles in NGC 3079 remains uncertain, as there is currently no conclusive evidence supporting whether they are driven by an AGN or by starburst winds. Interestingly, from the point of view of the ionised gas mass they are comparable to M82 and NGC 1068 though with 10 times larger kinetic energy (Veilleux et al., 1994).

We are not aware of any other well-defined bubbles in nearby disk galaxies that do not appear to be driven primarily by galactic nuclear starbursts. Nevertheless, the above comparison of the three bipolar structures suggests a trend of decreasing plasma temperature with increasing size. We then hope to gain insight into this and possible other trends from comparison with computer simulations of such structures.

4.4   Comparison with simulations

We focus this comparison on galactic bubble structures simulated in a cosmological context. Based on the study of 127 TNG50 simulated Milky Way/M31-like galaxies viewed edge-on, Pillepich et al. (2021) have identified large-scale high-pressure features that are morphologically similar to the eROSITA/Fermi bubbles. Such features are present in about 2/3 of the simulated galaxies and often appear in more or less symmetrical pairs above and below the galactic disks. Some of the galaxies contain multiple bubbles or shells with increasing sizes away from the galactic disks, resulting from multiple energetic energy releases from the accreting SMBH every 20-50 Myr. The global morphology of the features is not sensitive to the exact form of the energy release (jets or winds from hot AGN accretion). However, only a small fraction of the features have extents smaller than 10 kpc. There are hardly any bubbles with extents $\lesssim 5$ kpc, but $\gtrsim 2.5$ kpc – the smallest extent at which the identification is made. This trend can be understood because the growth of a bubble generally slows down with increasing extent – resulting in an increasing probability of being seen. Therefore, small features like those seen in M106 and NGC 4438 are likely to be rare, which explains why few features similar to the M106 structure have been found in or around other nearby disk galaxies.

On the other hand, small features, although rare, should be easier to detect if they are well resolved in X-ray observations. The surface intensity of a bubble generally decreases with its extent. While

the predicted brightness is typically $\lesssim 10^{35-36}$ erg s^{-1} kpc^{-2} for the simulated bubbles (with their extents typically $\gtrsim 10$ kpc), compared to $\sim 4 \times 10^{36}$ erg s^{-1} kpc^{-2} for the eROSITA bubbles (extent ~ 14 kpc), $\sim 4 \times 10^{38}$ erg s^{-1} kpc^{-2} for the M106 bubbles (~ 8 kpc), or $\sim 3 \times 10^{40}$ erg s^{-1} kpc^{-2} for the northwest nuclear bubble (~ 0.3 kpc) in NGC 4438 (Machacek et al., 2004; Li et al., 2022). Thus it is empirically evident that the surface brightness of a bubble decreases rapidly with its expansion.

In the work of Pillepich et al. (2021) the plasma temperature is characterized by mass-weighted values, typically in the range of T$\approx 10^{6.4-7.2}$ K. This range is not inconsistent with the values given above for the observed features (§ 4.3). However, it should be noted that the temperatures estimated from the spectral fits are biased toward lower values if the X-ray emitting plasma is not isothermal.

Furthermore, our X-ray spectral results show that the mean plasma temperature tends to be lower at the edges than inside the bubbles Tables 5 and 6, especially when its anticorrelation with σ_x is taken into account. This trend indicates that the velocity of the outer shock, if largely responsible for the heating of the plasma, has decreased with time. This is expected for a superbubble expanding into the CGM, similar to the scenario proposed for the eROSITA/Fermi bubbles (e.g., Mou et al., 2014). In this case, the ejected material from galactic central regions, most likely solar or supersolar, has been largely diluted by the heated CGM, which may well be sub-solar (e.g., Ursino et al., 2016; Miller & Bregman, 2016; Kataoka et al., 2018). The metallicity of the simulated bubble is in the range of 0.5-2 $Z_\odot$, consistent with $\sim 0.42 Z_\odot$ and 0.76 $Z_\odot$ for the E and W bubbles within the uncertainties of the estimates (Table 4); the emission measured-weighted metallicity is also expected to be biased toward lower values. Lower metal abundances ($\sim 0.2 Z_\odot$) are obtained for the eROSITA/Fermi bubbles (e.g., Kataoka et al., 2018).

As shown in the TNG50 simulations, such energetic bubbles are produced by feedback from AGNs with Eddington ratios of typically $\sim 10^{-5} - 10^{-4}$ (Pillepich et al., 2021). The misalignment between the jets and the general orientation of the bubbles in M106 also does not seem to be a problem in this AGN feedback scenario. For example, simulations of Sarkar et al. (2022) show that jets in a disk galaxy tend to be locally strangulated, producing high-pressure expanding cocoons. The overall morphology of the resulting large-scale bubbles is mostly determined by the distribution of the surrounding medium (i.e., the ISM and the CGM), not by the direction of the jets.

Therefore, the observations are in broad agreement with the simulations with respect to the size dependence of the observed probability, the X-ray morphology and surface intensity, and the temperature and metallicity of the superbubble structures in nearby galaxies.

4.5   Origin of the M106 structure

Based on the above comparisons, we now discuss what might have powered the M106 structure. The supermassive black hole of the AGN in the galaxy is surrounded by a molecular disk undergoing Keplerian motion, as traced by masers observed through very long baseline interferometry. The measured mass of the black hole is 4×10^7 M$_\odot$ (Nakai et al., 1993; Miyoshi et al., 1995). Extensive X-ray studies of the AGN have been carried out (e.g., Makishima et al., 1994; Lasota et al., 1996; Yuan et al., 2002; Véron-Cetty & Véron, 2006; Masini et al., 2022). The recent study by Masini et al. (2022) shows that the X-ray properties of the AGN fluctuate on timescales of hours to years, both intrinsically and due to absorption.

The intrinsic 2-10 keV luminosity was $\sim 10^{41}$ erg s^{-1} in the early 2000s, but decreased by a factor of ~ 3 by 2016. The low Eddington ratio ($\sim 10^{-4}$) of the AGN is well within the regime expected for a radiatively inefficient accretion flow, which tends to release mechanical energy by jets (Yuan et al., 2002). With the energy release, $\sim 10^{37}$ erg s^{-1}, inferred from the observed jets (Krause et al., 2007), the AGN would have to have lasted $\sim 10^{9}$ yrs just to accumulate the thermal energy of the bubbles. However, the jets could be much more powerful in the recent past and/or the power of the AGN is dominated by the wind from the hot accretion – a scenario quite similar to that proposed for the eROSITA/Fermi bubbles (e.g., Mou et al., 2014).

Alternatively, the M106 structure could be driven primarily by the energy release from stellar feedback, mainly via supernovae (SN). Ogle et al. (2014) estimate a total stellar mass of 8×10^{9} M$_\odot$ and a moderate star formation rate of ~ 0.08 M$_\odot$ yr^{-1} in the central 3.4 kpc^2 of the galaxy, which are comparable to the values (within their uncertainties) found at the central region of our Galaxy (e.g., Henshaw et al., 2022). Therefore, we may adopt its estimated SN rate $\sim (2 - 15) \times 10^{-4}$ yr^{-1} or the corresponding mechanical energy release of $(0.6 - 5) \times 10^{40}$ erg s^{-1}, assuming 10^{51} erg per SN (Crocker et al., 2011; Ponti et al., 2015). Therefore, if only a small fraction of this energy (e.g., 10% via accelerated relativistic particles alone; Crocker et al. (2011)) may escape the central disk region, then the SN feedback may be responsible for much of the thermal energy observed in the M106 bubbles. Furthermore, if both the energy input rate and the ambient medium properties are similar, then the age (t) of the M106 structure should be a factor of ~ 3 to 6 smaller than the the eROSITA/Fermi bubbles, if $t \propto R^{5/3}$ to $R^{5/2}$ (from steady to explosive energy input), where R is the characteristic radius/extent of a bubble (e.g., Mac Low & McCray, 1988). However, this stellar feedback origin may have difficulty to explain the discrete nature of the bubbles. M106 is clearly not a nuclear starburst galaxy; in fact, the study by Ogle et al. (2014) suggests that much of the gas in the central region of the galaxy has been ejected into the halo because of the recent AGN. Also no similar energetic radio/X-ray structures have been observed in extensive surveys of nearby highly-inclined disk galaxies with comparable or higher star formation rates (e.g. Wiegert et al., 2015; Li & Wang, 2013; Li et al., 2017).

Therefore, we favor the recent AGN origin of the M106 structure, although the fate of the SN energy release in galactic disks remains an interesting question to answer (e.g., Wang, 2010).

5 Summary

We have presented the discovery and analysis of a pair of radio/X-ray bubbles located above and below the disk of the nearby disk galaxy M106, using the recently released LoFAR survey data in the 120-168 MHz and 42-66 MHz bands and the Chandra data archive. Our study includes spatial and spectral analyses of the radio and X-ray data to understand the properties of the bubbles and compare them with those from the eROSITA/Fermi bubbles observations and cosmological simulations. Our main findings are summarized as follows:

- The bipolar structure of M106 includes the diffuse radio and X-ray emissions from the bubbles and their two unilaterally enhanced edges (Fig. 9). These edges were previously known as two anomalous arms of the galaxy, and together they form an S-shape, which is quite different from the one-sided (Galactic northeast) enhancement (i.e., the Radio Loop I and X-ray NPS) observed in the eROSITA/Fermi bubbles. The M106 structure extends ~ 8 kpc away from the galactic disk of M106 and is physically a factor of ~ 2 smaller than the eROSITA bubbles.

- The radio and X-ray emissions from the M106 structure show a general morphological similarity, suggesting that they are physically associated or coexist in the bubbles. However, there is a lack of detailed correspondence between radio and X-ray substructures, indicating that they can be produced independently. Some of the substructures may just represent features projected inside the bubbles.

- The radio spectral index map constructed from the LoFAR data clearly shows that the radio emission is non-thermal and thus synchrotron in origin. The index has a mean value of ~ 1. Assuming the energy equipartition between the cosmic ray and magnetic field, we estimate the mean magnetic field strength to be $\sim 3 - 4\,\mu G$ at the bubble centers and up to $\sim 13\,\mu G$ at the edges.

- The spectral index and the intensity of the radio emission further shows an anti-correlation in the bubbles. This anti-correlation is absent in the off-bubble galactic disk regions and is naturally explained by the synchrotron cooling of the cosmic-ray electrons in the bubbles. This explanation, together with the equipartition field strength, places an age limit of the M106 structure to be greater than $\sim 1 \times 10^8$ yrs.

- The X-ray spectra of the bubbles can be reasonably well characterized as an optically thin thermal plasma with a lognormal temperature distribution with a mean at ~ 0.2 keV and a dispersion $\sigma(\ln T) \sim 1$. The E/W bubble interiors have the luminosities of $\sim 4.7/7.7 \times 10^{39}$ erg s^{-1}, the thermal energy of $1.8/1.7 \times 10^{56}$ erg, and the mean cooling time scale of 1.3/0.7 Gyr. Compared to the cosmic ray/magnetic field, the thermal plasma seems to dominate the pressure and thus the force driving the expansion of the bubbles. The metal abundance of the plasma appears to be sub-solar, suggesting that the bulk of the plasma is the heated CGM of low metallicity, diluting the chemical enrichment of the ejected material from the central region of the galaxy.

- Our results are broadly consistent with those expected from the TNG50 simulations (e.g., Pillepich et al., 2021) and indicate that the M106 structure is the result of a relatively recent and powerful feedback episode of the AGN, although a stellar feedback origin cannot be completely ruled out. Older and larger structures may be present in the galaxy's CGM.

- In fact, the Chandra data also show evidence of diffuse X-ray emission from the galaxy on scales larger than the bipolar superbubble structure. However, both the counting statistics and the spatial coverage of the data are too limited to allow a detailed analysis of this large-scale hot CGM.

- The M106 structure is apparently a younger version of the eROSITA/Fermi bubbles, probably similarly powered and evolved in a comparable galactic environment, but allows a view with considerably less or different confusion with the galactic disk material.

While the present work was initially motivated by the striking appearance of the radio bubbles of M106 in the LoFAR DR2 release, more about the presence of galactic nuclear outflow structures could be revealed by a systematic survey of the X-ray data archive (including the release of the eROSITA sky survey data in the near future), as well as the available LoFAR data in both the 120-168 MHz and 42-66 MHz bands. Future deeper high-resolution observations with broader field coverage may further reveal larger scale dome-like or cocoon-like features around nearby disk galaxies providing important insights into the role of galactic feedback in regulating the structure and evolution of the CGM.

Bibliography

Basu A., Beck R., Schmidt P., Roy S., 2015, Mon. Not. R. Astron. Soc., 449, 3879

Beck R., Krause M., 2005, Astronomische Nachrichten, 326, 414

Berkhuijsen E. M., 1971, Astron. Astrophys., 14, 359

Bondi H., 1952, Mon. Not. R. Astron. Soc., 112, 195

Bragg A. E., Greenhill L. J., Moran J. M., Henkel C., 2000, Astrophys. J., 535, 73

Burbidge E. M., Burbidge G. R., Prendergast K. H., 1963, Astrophys. J., 138, 375

Carretti E., et al., 2013, Nature, 493, 66

Cecil G., Wilson A. S., de Pree C., 1995, Astrophys. J., 440, 181

Cecil G., et al., 2000, Astrophys. J., 536, 675

Cheng Y., Wang Q. D., Lim S., 2021, Mon. Not. R. Astron. Soc., 504, 1627

Cimatti A., Fraternali F., Nipoti C., 2019, arXiv e-prints, p. arXiv:1912.06216

Claussen M. J., Heiligman G. M., Lo K. Y., 1984, Nature, 310, 298

Crocker R. M., Jones D. I., Aharonian F., Law C. J., Melia F., Oka T., Ott J., 2011, Mon. Not. R. Astron. Soc., 413, 763

Crocker R. M., Bicknell G. V., Taylor A. M., Carretti E., 2015, The Astrophysical Journal, 808, 107

Das K. K., Zucker C., Speagle J. S., Goodman A., Green G. M., Alves J., 2020, Mon. Not. R. Astron. Soc., 498, 5863

Delvecchio I., et al., 2021, Astron. Astrophys., 647, A123

Fabian A. C., 2012a, Annu. Rev. Astron. Astrophys., 50, 455

Fabian A. C., 2012b, Annu. Rev. Astron. Astrophys., 50, 455

Gillessen S., Eisenhauer F., Trippe S., Alexander T., Genzel R., Martins F., Ott T., 2009, Astrophys. J., 692, 1075

Guo F., Mathews W. G., 2012, Astrophys. J., 756, 181

HI4PI Collaboration et al., 2016, Astron. Astrophys., 594, A116

Harris D. E., Grindlay J. E., 1979, Mon. Not. R. Astron. Soc., 188, 25

Heald G., et al., 2011, Astron. Astrophys., 526, A118

Heald G. H., et al., 2015, Astron. Astrophys., 582, A123

Heckman T. M., Best P. N., 2014, Annu. Rev. Astron. Astrophys., 52, 589

Henshaw J. D., Barnes A. T., Battersby C., Ginsburg A., Sormani M. C., Walker D. L., 2022, arXiv e-prints, p. arXiv:2203.11223

Hickox R. C., Alexander D. M., 2018, Annu. Rev. Astron. Astrophys., 56, 625

Hopkins P. F., Kereš D., Oñorbe J., Faucher-Giguère C.-A., Quataert E., Murray N., Bullock J. S., 2014, Mon. Not. R. Astron. Soc., 445, 581

Hyman S. D., Calle D., Weiler K. W., Lacey C. K., Van Dyk S. D., Sramek R., 2001, Astrophys. J., 551, 702

Ishibashi W., Fabian A. C., 2016, Mon. Not. R. Astron. Soc., 457, 2864

Israel F. P., Mahoney M. J., 1990, Astrophys. J., 352, 30

Kataoka J., Sofue Y., Inoue Y., Akita M., Nakashima S., Totani T., 2018, Galaxies, 6, 27

Krause M., Fendt C., Neininger N., 2007, Astron. Astrophys., 467, 1037

Laine S., Krause M., Tabatabaei F. S., Siopis C., 2010, Astron. J., 140, 1084

Large M. I., Quigley M. J. S., Haslam C. G. T., 1962, Mon. Not. R. Astron. Soc., 124, 405

Lasota J. P., Abramowicz M. A., Chen X., Krolik J., Narayan R., Yi I., 1996, Astrophys. J., 462, 142

Li J.-T., Wang Q. D., 2013, Mon. Not. R. Astron. Soc., 428, 2085

Li J.-T., Bregman J. N., Wang Q. D., Crain R. A., Anderson M. E., Zhang S., 2017, Astrophys. J. Suppl. Ser., 233, 20

Li J.-T., Hodges-Kluck E., Stein Y., Bregman J. N., Irwin J. A., Dettmar R.-J., 2019, Astrophys. J., 873, 27

Li J.-T., et al., 2022, Mon. Not. R. Astron. Soc., 515, 2483

Mac Low M.-M., McCray R., 1988, Astrophys. J., 324, 776

Machacek M. E., Jones C., Forman W. R., 2004, Astrophys. J., 610, 183

Makishima K., et al., 1994, Publ. Astron. Soc. Jpn, 46, L77

Martig M., Bournaud F., Teyssier R., Dekel A., 2009, Astrophys. J., 707, 250

Masini A., Wijesekera J. V., Celotti A., Boorman P. G., 2022, Astron. Astrophys., 663, A87

McKee C. F., Ostriker J. P., 1977, Astrophys. J., 218, 148

Miller M. J., Bregman J. N., 2016, Astrophys. J., 829, 9

Miyoshi M., Moran J., Herrnstein J., Greenhill L., Nakai N., Diamond P., Inoue M., 1995, Nature, 373, 127

Mou G., Yuan F., Bu D., Sun M., Su M., 2014, Astrophys. J., 790, 109

Mou G., Wu J., Sofue Y., 2022, arXiv e-prints, p. arXiv:2212.04306

Mou G., et al., 2023, Nature Communications, 14, 781

Murphy E. J., 2009, Astrophys. J., 706, 482

Nakai N., Inoue M., Miyoshi M., 1993, Nature, 361, 45

Ogle P. M., Lanz L., Appleton P. N., 2014, Astrophys. J. Lett., 788, L33

Panopoulou G. V., Dickinson C., Readhead A. C. S., Pearson T. J., Peel M. W., 2021, Astrophys. J., 922, 210

Pillepich A., Nelson D., Truong N., Weinberger R., Martin-Navarro I., Springel V., Faber S. M., Hernquist L., 2021, Mon. Not. R. Astron. Soc., 508, 4667

Ponti G., et al., 2015, Mon. Not. R. Astron. Soc., 453, 172

Predehl P., et al., 2020, Nature, 588, 227

Rybicki G. B., Lightman A. P., 1986, Radiative Processes in Astrophysics

Sarkar K. C., Mondal S., Sharma P., Piran T., 2022, arXiv e-prints, p. arXiv:2211.12967

Schawinski K., et al., 2014, Mon. Not. R. Astron. Soc., 440, 889

Shakura N. I., Sunyaev R. A., 1973, Astron. Astrophys., 24, 337

Shimwell T. W., et al., 2017, Astron. Astrophys., 598, A104

Shimwell T. W., et al., 2019, Astron. Astrophys., 622, A1

Shimwell T. W., et al., 2022, Astron. Astrophys., 659, A1

Smith R. K., Brickhouse N. S., Liedahl D. A., Raymond J. C., 2001, Astrophys. J. Lett., 556, L91

Snowden S. L., et al., 1995, Astrophys. J., 454, 643

Su M., Slatyer T. R., Finkbeiner D. P., 2010, Astrophys. J., 724, 1044

Tumlinson J., Peeples M. S., Werk J. K., 2017, Annu. Rev. Astron. Astrophys., 55, 389

Ursino E., Galeazzi M., Liu W., 2016, Astrophys. J., 816, 33

Veilleux S., Cecil G., Bland-Hawthorn J., Tully R. B., Filippenko A. V., Sargent W. L. W., 1994, Astrophys. J., 433, 48

Véron-Cetty M. P., Véron P., 2006, Astron. Astrophys., 455, 773

Vijayan A., Li M., 2022, Mon. Not. R. Astron. Soc., 510, 568

Wang Q. D., 2010, Proceedings of the National Academy of Science, 107, 7168

Wang Q. D., Zeng Y., Bogdán Á., Ji L., 2021, Mon. Not. R. Astron. Soc., 508, 6155

Wiegert T., et al., 2015, Astron. J., 150, 81

Wilson A. S., Yang Y., Cecil G., 2001, Astrophys. J., 560, 689

Woo J.-H., Urry C. M., 2002, Astrophys. J., 579, 530

Yang Y., Li B., Wilson A. S., Reynolds C. S., 2007, Astrophys. J., 660, 1106

Yang H. Y. K., Ruszkowski M., Ricker P. M., Zweibel E., Lee D., 2012, Astrophys. J., 761, 185

Yang H. Y. K., Ruszkowski M., Zweibel E. G., 2022, Nature Astronomy, 6, 584

Yuan F., Markoff S., Falcke H., Biermann P. L., 2002, Astron. Astrophys., 391, 139

Zubovas K., Bourne M. A., 2017, Mon. Not. R. Astron. Soc., 468, 4956

Zubovas K., Nayakshin S., 2012, Mon. Not. R. Astron. Soc., 424, 666

de Gasperin F., et al., 2023, arXiv e-prints, p. arXiv:2301.12724

van der Kruit P. C., Oort J. H., Mathewson D. S., 1972, Astron. Astrophys., 21, 169

Appendices

A   Spectral analysis of the local X-ray background

We fit the local background spectrum with a model comprising of various expected components (Eq. 7):

$$APEC_{LB} + TBABS(APEC + POWERLAW), \tag{7}$$

where APEC the plasma model same as the VAPEC, but with the metal abundances fixed to the default solar values in Xspec. The APEC model represents collisional-ionized plasma and depending on four parameters: temperature, abundance, redshift, and normalizatiom and here we fit the parameters for temperature and normalization only. The TBABS model characterizes the foreground hydrogen column density. The POWERLAW model is a standard power law parameterized by the photon index and normalization. The $APEC_{LB}$ component in our model represents the contribution from the Local Bubble with a fixed temperature of 0.1 keV (Smith et al., 2001)., while the combination of APEC and POWERLAW characterizes the background emission from more distant contributions from diffuse hot gas and unresolved point-like sources, chiefly AGNs. This emission is subject to the Galactic foreground absorption (TBABS) with a hydrogen column density of $N_H = 4.2 \times 10^{20}$ cm^{-2} in the direction of M106 (HI4PI Collaboration et al., 2016). The fitting is satisfactory ($\chi^2/dof = 20/22$) and gives the Xspec normalizations of the as $0.246^{+0.05}_{-0.03}$, $1.73^{+7.87}_{-5.57}$, and $8.82^{+2.96}_{-3.00}$ for the $APEC_{LB}$, APEC and power law, as well as the APEC temperature as $4.54^{+2.65}_{-3.37}$.